4-20-2012

QUASAR JETS ON PARSEC AND KILOPARSEC SCALES

Gareth Jones
Trinity University, gjones1@trinity.edu

QUASAR JETS ON PARSEC AND KILOPARSEC SCALES
GARETH JONES

A DEPARTMENT HONORS THESIS SUBMITTED TO THE
DEPARTMENT OF PHYSICS & ASTRONOMY AT TRINITY UNIVERSITY
IN PARTIAL FULFILLMENT OF THE REQUIREMENTS FOR GRADUATION WITH
DEPARTMENTAL HONORS

DATE APRIL 20, 2012

_____ _____
THESIS ADVISOR DEPARTMENT CHAIR

_____
ASSOCIATE VICE PRESIDENT FOR ACADEMIC AFFAIRS,
CURRICULUM AND STUDENT ISSUES

Abstract

In order to improve our understanding of the physics of relativistic jets in quasars, we examined correlations originally reported by Bridle *et al*. (1994). We expanded their original sample of 13 3CR lobe-dominated quasars imaged by the VLA to a statistically complete sample of 21. Using the NRAO AIPS image analysis software, we measured structural parameters and flux densities for various quasar features. A previous correlation between the prominences (relative brightness) of the straight kiloparsec-scale jet and the central feature was strengthened by the inclusion of additional sources. In the relativistic beaming interpretation, the slope of this correlation indicates jet deceleration to $\gamma \sim 2$ on large scales. A previous anticorrelation between the bend angle of the jet and hot spot (jet terminal point) prominence was found to rely heavily on the single bizarre source 3C215; without this source, the anticorrelation is not statistically significant. Because the most prominent features of the jet (knots) are disturbances in the flow, the regions between them were examined as better measures of the continuous flow. It was found that the interknot regions and knots are each separately relativistically beamed and that the proportion of jet flux contained in the knots is not due to beaming. While the strength of interknot emission does not depend on distance from the central feature, knot peak flux density does decrease with distance. This suggests no deceleration in the interknot regions, which are then still relativistic when they interact with the lobe and thus supply considerable energy to power the lobe. As for the knots, either the mechanism behind shock formation weakens with distance from the central feature or the change in brightness is due to another, more complicated facet of shock physics. In order to place limits on the speed and orientation of the jets of the quasars in the sample, histograms of observed and theoretical distributions of jet/counterjet brightness ratios were examined, where it was found that $\gamma_{JET} \geq 3$ provided acceptable fits, although $\gamma_{JET} = 2$ would be acceptable if the source with the

highest jet/counterjet ratio was removed. Because only a small portion of the sample exhibited counterjet candidates, the distributions of jet brightness alone were also compared. Good fits were obtained for three different jet models, all with a restricted range of jet orientation angles: identical homogeneous jets with a single Lorentz factor, identical inhomogeneous jets with a fast central spine and slower outer sheath, and homogeneous jets with a single Lorentz factor and a range of intrinsic brightness. These models produced poor fits to the observed distribution for jets with random orientations. The comparison of transverse profiles with theoretical convolutions ruled out very fast and/or very low emissivity spines.

Acknowledgements

My deepest thanks to Dr. David Hough, whose inspiration and guidance made this project possible. As my advisor for the last four years, he provided me opportunities and the example that led me to undertaking this project. I am convinced that my undergraduate experience was made richer by his leadership and devotion to his field and students.

In addition, I would like to thank Dr. Alan Bridle for the foundation that he laid with Dr. Hough in their earlier work and for his assistance and his insight concerning this project.

I also thank the physics faculty of Trinity University for supporting me in my work and reviewing this paper, including Dr. Dennis Ugolini, Dr. Jennifer Steele, Dr.Gordon MacAlpine, Dr. Daniel Spiegel, Dr. Kelvin Cheng, and Dr. Nirav Mehta. Additionally, I thank Dr. Mark Lewis for allowing me to perform research in a different area.

Overall, I am grateful for the vision and resources of Trinity University and its support of this work.

This project was supported by an AAS Small Research Grant.

Contents

1 Introduction **1**

1.1 Historical Overview 1

1.2 Current AGN Model 3

2 Jet Theory **6**

2.1 Quasar Central Engine 6

2.2 Emission Mechanisms 7

2.3 Jet Powering Mechanisms 8

2.4 Knot Formation 9

2.5 Superluminal Motion 10

2.6 Doppler Beaming 11

3 Radio Interferometric Imaging **16**

3.1 Radio Interferometry 16

3.1.1 Source Structure from Fringe Frequency 17

3.1.2 Fourier Imaging 19

3.2 Radio Interferometry Arrays 20

3.3 Data Editing, Calibration, and Imaging 21

3.4 Image Analysis 23

4 Observational Results & Analysis **25**

4.1 Image Preparation and Feature Identification 25

4.1.1 Definitions 25

4.1.2 Images 26

4.2 Small- & Large-Scale Kinematics 35

4.3 Jet Bending 46
4.4 Interknot Emission 49
4.5 Number Distributions of Jet/Counterjet Brightness Ratios 56
4.6 Number Distributions of Jet Brightness 57
4.7 Transverse Brightness Profiles 66

5 Interpretation & Discussion **71**
5.1 Source Structure 71
5.2 Small- & Large- Scale Jet Connections 71
5.3 Jet Bend Angle - Hot Spot Prominence Relation 74
5.4 Interknot Emission 75
5.5 Jet/Counterjet Brightness Ratio 77
5.6 Jet Brightness Distributions 78
5.7 Transverse Jet Profiles 78

6 Conclusion **80**

References **82**

1 Introduction

1.1 Historical Overview

Active galactic nuclei (AGN) are known to be compact regions of high luminosity in the centers of galaxies. This identification and the unification it represents were made in steps over the past century. When Edward Fath recorded optical spectra of galaxies in 1908, the source NGC 1068 showed bright emission lines that did not match the absorption line spectra of the other sources, according to Carroll & Ostlie (2007). In 1943, Carl Seyfert found that broad emission lines originated from highly ionized atoms in the nuclei of galaxies and that these nuclei were similar to stars in appearance. The galaxies containing such nuclei are now known as Seyfert 1 and 2 galaxies, where Seyfert 1 galaxies exhibit broad permitted emission lines with narrow forbidden lines and a luminous continuum and Seyfert 2 galaxies exhibit narrow emission lines and a less luminous continuum. Because the centers of these galaxies exhibit a high degree of emission, they became known as active galactic nuclei.

In the early 1930s, Karl Jansky was assigned by Bell Laboratories to find sources of static that would be detrimental to communication made with radio waves, according to Ghigo (2008). After constructing an antenna that received signals at 20.5 MHz, Jansky found a steady background signal that repeated every 23 hours and 56 minutes, exactly the Earth's sidereal rotation period, which means it originated outside of our solar system. The source was found to be in the direction of the Milky Way center, which spurred further investigation of radio emissions. However, because of funding limitations during the Great Depression, new investigations were limited, and it was not until after World War II that significant progress was made. One of these new investigations revealed the strong radio source Cygnus A. It was optically identified as an elliptical galaxy at a distance of 240 Mpc, which shows that it must have high radio luminosity, as it is the brightest radio source outside the Milky

Way. Thus, Cygnus A was the first galaxy to be classified as a "radio galaxy," or galaxy that exhibits a high degree of radio emission. This class is further divided into broad-line radio galaxies (BLRGs), which are similar in emission properties to Seyfert 1 galaxies, and narrow-line radio galaxies (NLRGs), which are similar to Seyfert 2 galaxies.

In 1960, while searching for an optical source at the same location as the radio source 3C48, Thomas Mathews and Allan Sandage found a 16th-magnitude object with unidentifiable emission lines. Because the optical counterpart was similar in appearance to a star, the sources were termed quasi-stellar radio sources, or QSRs, which became the classification quasars. When the source 3C273 with a similarly odd spectrum was found in 1963, Maarten Schmidt discovered that its emission lines were those of the hydrogen Balmer lines, which had been redshifted. From this and the cosmological redshift formula $\frac{\Delta\lambda}{\lambda} = 1 + z$, the redshifts of 3C48 and 3C273 were found to be 0.367 and 0.158, respectively, which correlate to distances of 1290 Mpc and 630 Mpc, which made 3C48 one of the most distant objects discovered at that time.

Originally classified as a variable star by Cuno Hoffmeister in 1926, BL Lacertae exhibited brightness variations as large as a factor of 15 over a period of months (Price 2010). When it was investigated further in 1968, it was found to have a featureless continuum and to be surrounded by a halo with a similar spectrum to an elliptical galaxy, suggesting that it was a galactic nucleus. Thus, BL Lac became the first of a subclass of blazars, or rapidly varying AGNs that are highly linearly polarized at optical wavelengths. So-called BL Lac objects exhibit the highest time variability of the blazar group.

Another classification made by B. L. Fanaroff and J. M. Riley in 1974 is dependent on the ratio of the distance between the brightest spots on each side of the central feature to the full size of the source. If this ratio is below 0.5, the sources are classified as Fanaroff-Riley Class-I (FR-I), which exhibit two features called jets that are often curved, as defined in

Kembhavi & Narlikar Sec 9.3 (1999). If the ratio is above 0.5, the sources are classified as Fanaroff-Riley Class-II (FR-II), which have a single visible jet that is straight. FR-II sources are also more luminous than FR-I objects, with luminosity greater than $4 \cdot 10^{25}$ W/Hz/sr at 178 MHz.

1.2 Current AGN Model

The current standard model for an AGN is a supermassive black hole that is surrounded by an accretion disk, which is surrounded by an obscuring torus, as seen in Figure 1.1. Leaving the vicinity of the black hole on a path roughly orthogonal to the plane of the accretion disk is a jet. This jet consists of plasma that is moving relativistically, which results in strong beaming effects. There is also a magnetic field oriented along the axis of the jet around which charged particles gyrate. This produces synchrotron radiation, which is very powerful in the radio wave region of the spectrum. On a radio image, the central feature consists of a core near the black hole and any small-scale structure of the jet. As the jet extends from the central feature, it exhibits shock features called knots, which are disturbances in the flow. After flowing for thousands of parsecs, the jet encounters the intergalactic medium and forms a hot spot, or bright feature at the end of the jet. As it slows, the jet spreads into an area called the lobe, which surrounds the hot spot.

AGN are classified into different types by the orientation of the jet to our line of sight, the mass of the black hole, the accretion rate, its spin, and other characteristics. For example, blazar jets are oriented along our line of sight, while quasar jets are oriented at larger angles. In increasing angle between our line of sight and the jet direction, AGN are classified as Radio Loud Quasars, Broad Line Radio Galaxies, and Narrow Line Radio Galaxies. The sample of AGN that is studied in this thesis consists of Lobe-Dominated Quasars, which are

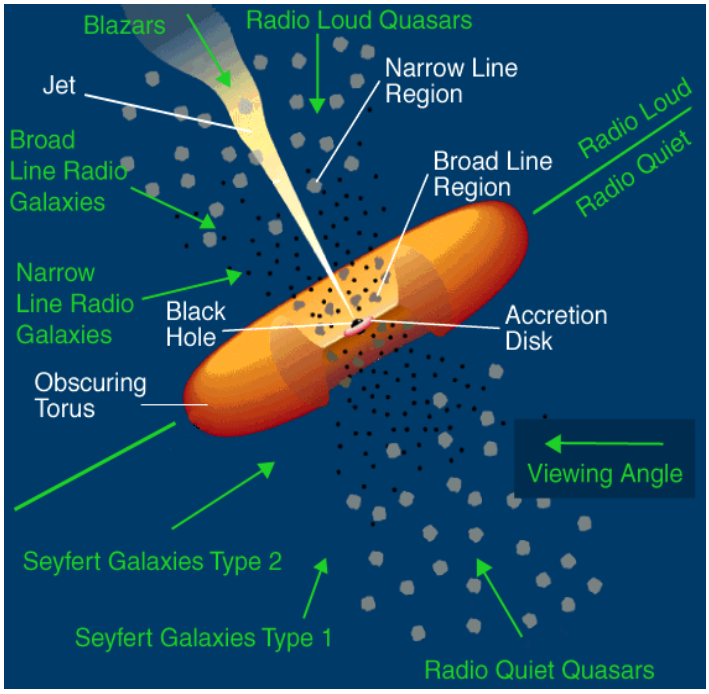

Figure 1.1: Illustration of active galaxy classification as function of angle of jet to line of sight. (Source: `http://www.auger.org/news/PRagn/about_AGN.html`)

thought to have large black holes with moderate accretion rates, high spin, and orientations of approximately 10^o-60^o to the line of sight. This angle range places Lobe-Dominated Quasars in the higher angle section of Radio Loud Quasars. This sample consists of FR II sources by luminosity; so only one jet is visible.

The primary goal of this thesis is to connect the large-scale (kiloparsec) quasar jet behavior to small-scale (parsec) jet structure. This was done by examining the relationships between the emission strengths of the straight portion of the jet and the central feature, the strength of the hot spot and the bend angle of the jet, the distribution of emission strengths of jets, the emission of jets between knots, and the relation between the emission strengths of the jet and counterjet. Chapter two will explain jet theory, including possible jet acceleration mechanisms, knot formation, and relativistic beaming. In chapter three, we will detail

the techniques utilized: radio interferometry, imaging, and statistical analysis. Our images and results will be presented in chapter four, and discussion of these results will be included in chapter five. We will conclude in chapter six.

2 Jet Theory

The main components of the standard model of galaxies with active galactic nuclei, or "active galaxies," are the central region, jets, and lobes. The central region consists of the central supermassive black hole, accretion disk, and jet formation zone. The jet travels outward over a distance of thousands of parsecs, interacting with the interstellar medium before terminating in the intergalactic medium in the lobe. The lobe itself is a magnetized plasma that accumulates at the end of the jet in a wide, diffuse structure.

2.1 Quasar Central Engine

It is generally accepted that quasars are powered by accretion around the central black hole. Evidence for the black hole includes the high degree of emission emanating from a small central area. If the brightness of a distant spherical source of emission with radius R changed suddenly, emission from the edge of the sphere would have to travel approximately R farther than emission from the center of the sphere, as seen in chapter 28.3 of Carroll & Ostlie (2007). Thus, the difference in emission would be observed over a time $\Delta t = R/c$. For sources at significant redshifts, this time is divided by the cosmological time dilation factor, so $R = \Delta t \cdot c/(1+z)$. As an example, for a time difference of one hour and $z = 0$, this means that the radius of the sphere of emission is 7.2 AU. The Eddington Luminosity, or largest luminosity for which the source remains in hydrostatic equilibrium, tells us that $L_{ED} = (1.5 \cdot 10^{31})\, W(M/M_{SOL})$, where M_{SOL} is the solar mass. Solving for M and assuming a typical quasar luminosity of $5 \cdot 10^{39}$ W gives the lower limit for the emission area mass as $3.3 \cdot 10^{8} M_{SOL}$. Using the radius of the emission area and solving the Schwarzschild radius for mass gives $M = (Rc^2)/(2G) = 3.7 \cdot 10^{8} M_{SOL}$. That the lowest mass required for hydrostatic equilibrium and the mass of a black hole with a Schwarzschild radius equal to the mass of

the emission area are so similar suggests that the emission area surrounds a black hole. The infalling material powering the quasar activity brings its angular momentum with it, so the material forms a rotating accretion disk around the black hole.

2.2 Emission Mechanisms

When electrons move in an environment with a magnetic field, they feel a magnetic force $\vec{F} = q(\vec{v} \times \vec{B})$ perpendicular to the direction of the magnetic field lines. If the velocity of an electron was mainly parallel to the field but contained a perpendicular component, it would be forced to move in a helix. The change of direction requires acceleration, so the electron emits synchrotron radiation. Because of this, jets, which are composed of a magnetized electron-positron or electron-proton plasma, contain particles that emit synchrotron radiation. This is seen in the main portions of the jet and in the knots, where a shock causes turbulence in the flow, delivering energy to the particles and enhancing their emission.

Compton scattering, or an elastic collision between high-energy photons and low-energy particles, results in higher energy particles. The opposite is also possible, as low-energy photons can be scattered to higher energies via collisions with high-energy particles, called inverse Compton scattering. Because of the abundance of high-energy particles in jets, this process may promote lower energy photons to x-ray or gamma emission.

Another important emission type is thermal emission, or radiation given off by particles at a certain temperature that follows a Planck curve. In the central region, accretion of matter onto the disk makes the disk material hot. This high temperature causes the central region to be very luminous. Additionally, because thermal radiation from a high temperature source spans a wide range of wavelengths, it contributes to emission in different bands, including radio. However, the overall spectrum of the nuclear region can only be explained

by accounting for both thermal and non-thermal (synchrotron) emission.

2.3 Jet Powering Mechanisms

One way that energy is added to the black hole system is through matter falling onto the accretion disk, converting gravitational potential energy to kinetic energy as the matter accelerates and collides with the disk. This addition of matter increases the rotational speed of the disk. Because the disk is ionized and acts as a conductor, this rotation creates a magnetic field around the disk. As the disk material moves and the magnetic field varies, an electric field is induced, which can transfer disk rotational energy to accelerate charged particles from the disk. Additionally, the central black hole acts as a conductor in a magnetic field, as an electromotive force is produced between its poles and its equator, which propels a stream of electron-positron pairs and electromagnetic radiation. As related by Carroll & Ostlie p.1115 (2007), this is the Blandford-Znajek mechanism and generates power $P = (4\pi/\mu_0)B^2R_s^2c$, where R_s is the Schwarzschild radius. This converts the rotational energy of the disk and black hole to power a relativistic outflow of charged particles.

Once away from the disk, the jet continues, so there must be a driving force that propels it to the terminal hot spot at the end of the jet. One possible source of energy is the radiation from the central feature. As this light collides with the charged particles of the jet material, the energy of particles can be upshifted via Compton scattering. If the light is scattered preferentially in the opposite direction of the jet travel, momentum conservation would demand that the particle travel in the direction of jet flow with a higher velocity than before the collision, as seen in O'Dell (1981). While this mechanism allows acceleration of jet material via radiation pressure, it is likely not the main propulsion source. Many models focus on magnetohydrodynamical (MHD) mechanisms, such as release of magnetic energy

in twisting field configurations.

Because the jet appears straight, there must be a collimating feature near the region of acceleration, as otherwise the jets could take shape as spherical outflows from the central feature, as shown in the introduction of Blandford & Rees (1974). This "nozzle" could be the magnetic field while the jet is close to the disk and the pressure of the interstellar and the intergalactic medium when away from the central feature. While the collimating forces lessen jet spreading, formation of knots and other inhomogeneities complicate the feature. Magnetic self-confinement by a current-carrying jet with a helical magnetic field, as seen in Benford (1983), is also a possibility.

2.4 Knot Formation

Evident in jets are areas of enhanced brightness, termed knots. In the case of a jet with varying initial acceleration conditions, groups of jet material that are accelerated to different speeds at different times have the possibility of catching up to one another. If these speeds are greater than the speed of sound, or wave propagation, in the jet material, the passage of faster material will result in the formation of a shock front, or simply "shock," as seen in Rees (1978). Because the shock is a result of the interaction of jet material with different speeds, it will advance with the jet material. For the simplified case of two regions of the jet considered by Stawarz *et al.* (2004) with $\gamma_2 > \gamma_1 > 1$, the shock will move with $\gamma_{shock} = \sqrt{\gamma_1 \cdot \gamma_2}$ both in the direction of jet propagation and against it. This will create a symmetric double shock of width $\Delta L = 2c\beta_{shock}\Delta t$, where Δt is the time that the shock has existed. Because of their creation by shock waves, they act as disturbances in the jet flow and thus have a different appearance than the underlying jet emission.

2.5 Superluminal Motion

When a source of emission moves relativistically with velocity components parallel and perpendicular to our line of sight, its transverse velocity may appear to be higher than c. This is a result of the source moving closer to the observer at an appreciable fraction of the speed of light, so light emitted closer to the observer travels a shorter distance than earlier emission. Thus, if the time and projected transverse displacement between the receipt of these emissions were used to find the speed of the source of emission, the velocity would not reflect the true velocity.

As an example, consider the situation depicted in Figure 2.1. At time $t = 0$ in the observer's frame, a blob in a quasar jet emits a photon that travels from A towards B. The blob moves then from A to C in time t_1, a distance of vt_1, and emits another photon at time t_1 at point C. If the distance from A to the observer is D, the photon from A will be received at time $t_A = D/c$, while the photon from C will be received

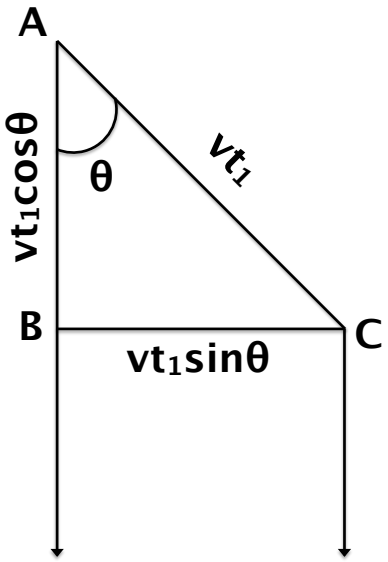

Figure 2.1: Apparent Superluminal Velocity.

at time $t_C = t_1 + (D - vt_1 cos\theta)/c$. The difference between these times will be $\delta t = t_1(1 - (v/c)cos\theta)$, so the apparent transverse velocity will be $v_{app} = (vsin\theta)/(1 - (v/c)cos\theta)$.

As an example, for $\theta = 45^O$ and $v = 0.98c$, $v_{app} = 6.77 \cdot 10^8 m/s = 2.26c$, according to p.1127 of Carroll & Ostlie (2007). Thus, apparent superluminal motion is possible in a sample of quasars.

2.6 Doppler Beaming

For a point source of light moving relativistically that emits isotropically in its rest frame, the observed flux density is strongly beamed in the forward direction. To see this, recall from the derivation of superluminal motion, $\Delta t_{obs} = \Delta t_{rest}\gamma(1 - \beta cos\theta)$, where Δt_{rest} is in the source's frame. With the substitution of the Doppler factor, $\delta = (\gamma(1 - \beta cos\theta))^{-1}$, this becomes

$$\Delta t_{obs} = \Delta t_{rest}/\delta \tag{1}$$

Because there is an inverse relationship between time and frequency, $\nu_{obs} = \delta\nu_{rest}$, and thus $\Delta\nu_{obs} = \delta\Delta\nu_{rest}$. Because the energy of a photon is proportional to frequency,

$$E_{obs} = \delta E_{rest} \tag{2}$$

Flux density is measured in $\frac{J}{s \cdot m^2 \cdot Hz}$, so the energy term contributes a factor of δ, the time term supplies a factor of δ, and the bandwidth term removes a factor of δ. The time and bandwidth terms nullify each other because more flux is received in a smaller period of time, but it is spread over a broader range of frequencies. Thus, because the receiving area is constant, the total effect due to energy, time, and frequency transformations is

$$S_{obs} = \delta S_{rest} \tag{3}$$

For a frame moving with relative velocity u toward the observer, the y' component of an object's velocity y' is $v'_{y'} = sin\theta' v'$, so

$$sin\theta' = \frac{v'_{y'}}{v'} \tag{4}$$

and similarly,

$$cos\theta' = \frac{v'_{x'}}{v'} \tag{5}$$

For the observer's frame,

$$sin\theta = \frac{v_y}{v} \tag{6}$$

For light, $v = v' = c$, so by the relativistic velocity addition equation,

$$sin\theta = \frac{v'_{y'}}{c\gamma(1 + \frac{uv'_{x'}}{c^2})} \tag{7}$$

By substituting $\beta = u/c$ and the expression for $v'_{x'}$, this becomes

$$sin\theta = \frac{v'_{y'}}{c\gamma(1 + \beta cos\theta')} \tag{8}$$

Using the expression for $v'_{y'}$,

$$sin\theta = \frac{sin\theta'}{\gamma(1 + \beta cos\theta')} \tag{9}$$

To solve for $sin\theta'$, a change in the sign of β would occur, all unprimed values of θ would become primed, and vice versa. Thus,

$$sin\theta' = \frac{sin\theta}{\gamma(1 - \beta cos\theta)} = \delta sin\theta \tag{10}$$

In the case of a high value of γ and a small value of θ, which describes relativistic jets oriented towards an observer, the value of δ will be high. Thus, due to the relation stated earlier, $\theta' > \theta$, which shows that light emitted at larger angles relative to our line of sight in the source's rest frame will be received at smaller angles.

An annulus in the observer's frame with differential angular width $d\theta$ occupies a differential solid angle $d\Omega = 2\pi sin\theta d\theta$, while a similar annulus in the source's rest frame occupies a differential solid angle $d\Omega' = 2\pi sin\theta' d\theta'$. Using Equation (10) and assuming small values of θ and θ', $\theta' = \delta\theta$, and $d\theta' = \delta d\theta$, by differentiation. Thus,

$$\frac{d\Omega'}{d\Omega} = \frac{sin\theta' d\theta'}{sin\theta d\theta} = \frac{\delta sin\theta \delta d\theta}{sin\theta d\theta} = \delta^2 \tag{11}$$

or $d\Omega' = \delta^2 d\Omega$. Therefore, by combining the effects of the transformations of energy, time, frequency, and solid angle,

$$S_{obs} = \delta^3 S_{em} \tag{12}$$

In a continuous jet, an area of rest length dl' will be contracted to $dl = \frac{dl'}{\gamma}$ by relativistic effects. This contraction would decrease the apparent size of the emitting area, increasing the brightness by a factor of γ, which is equal to $1/\delta$ when $\theta = 90^o$. Since the flux density of an area of jet material is then generally increased by a factor of δ for any angle, $S_{obs} = S_{em}/\gamma^2 = \delta^2 S_{em}$. However, emission from point sources ("blobs") is not affected by this contraction, so $S_{obs} = S_{em}/\gamma^3 = \delta^3 S_{em}$.

Flux density follows a power law,

$$S \propto \nu^{-\alpha} \tag{13}$$

where α is the spectral index. If light is emitted at frequency ν_{em} and observed at a frequency

ν_{obs},

$$\frac{S_{em}(\nu_{em})}{S_{em}(\nu_{obs})} = \frac{C\nu_{em}^{-\alpha}}{C\nu_{obs}^{-\alpha}} = (\frac{\nu_{em}}{\nu_{obs}})^{-\alpha} \tag{14}$$

where C is a constant. From Equation (2), $\frac{\nu_{em}}{\nu_{obs}} = \delta^{-1}$. This relation makes $\frac{S_{em}(\nu_{em})}{S_{em}(\nu_{obs})} = \delta^{-\alpha}$.

If this effect is added to those of Equation (6),

$$S_{obs}(\nu_{obs}) = \delta^{2+\alpha} S_{em}(\nu_{obs}) \tag{15}$$

for a continuous jet. This correction is made so that flux densities can be compared at a common rest frame frequency.

In the case of jet material with spectral index 0.6 moving at $0.98c$, the beamed flux density can be orders of magnitude more powerful than the rest flux density, if the velocity

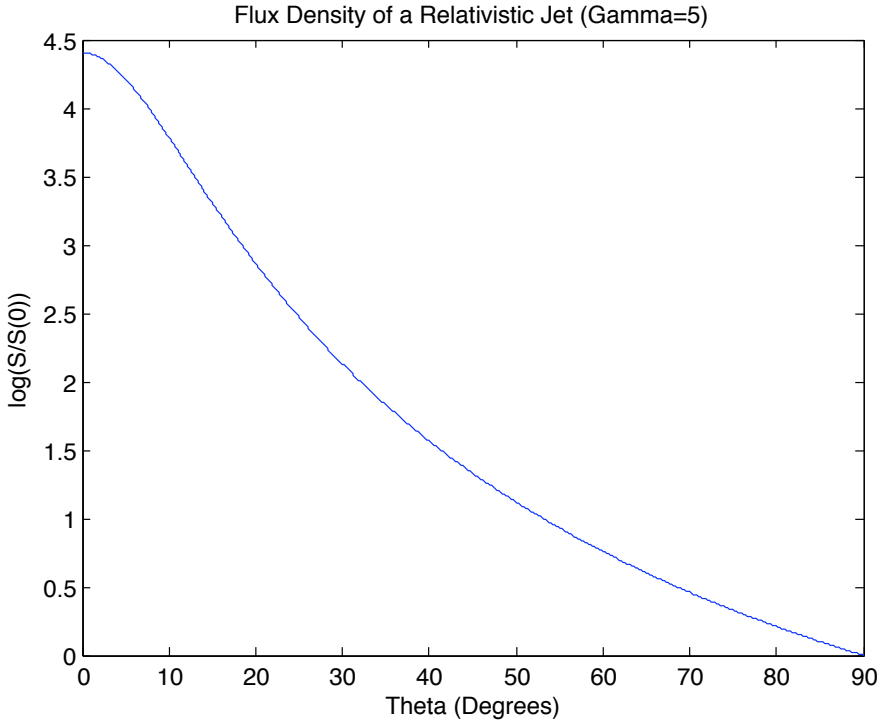

Figure 2.2: Beamed flux density of a relativistic jet ($\gamma = 5$).

is directly towards the observer (Figure 2.2). If the velocity is perpendicular to the line of sight, the observed signal is very weak.

3 Radio Interferometric Imaging

The basic interferometer (*i.e.*, the Michelson interferometer) splits light along two paths (arms), reflects them, recombines them, and outputs their interference pattern. As the path lengths of the arms change, light travels a different distance, so it has a different phase when it reaches the point of interference. Thus, when the light from each arm constructively interferes, a bright fringe is observed, while destructive interference produces a dark fringe. This device allows one to measure changes in arm length precisely. While radio interferometry uses a different setup, the underlying principles of interference for different "arm lengths" - telescope separations - is the same.

3.1 Radio Interferometry

In 1962, Ryle and Neville, two researchers at the Cavendish Laboratory, showed that a single pair of telescopes (also called antennas), if connected as an interferometer, could provide coverage of a source if observations were continued while the Earth rotates. Over a single rotation, the projected distance between the telescopes (the "baseline") would change from the viewpoint of the source. The use of the Earth's rotation to sample baselines over a period of time is called aperture synthesis.

In radio astronomy, the angular resolution of an aperture with diameter D observing at wavelength λ is $\theta = \lambda/D$. Because radio waves have long wavelengths, we must have a large aperture. Since it is impractical to construct a continuous 1000 km dish (or even a 1 km dish), the use of interferometry allows observation with acceptable resolution. Using an array of telescopes at different separations (baselines), we can create an aperture that has an effective diameter of the maximum separation of the telescopes, which can be tens to thousands of kilometers.

3.1.1 Source Structure from Fringe Frequency

Figure 3.1 depicts a two-telescope array with baseline D observing two point sources A and B. In the case of a single point source, the emitted wavefronts must travel farther to reach one telescope than the other, resulting in a path length difference. If compared to a Young double slit experiment where the telescopes are the slits, this path length difference results in fringes in the interference output. A system of radio telescopes handles a pair of signals by multiplying them and recording the strength of the central fringe. Thus, as the source moves across the sky, we observe the central fringe going through a brightness cycle at a frequency called the fringe frequency, or the frequency at which the central fringe moves from one maximum to the next.

In the case of two antennas (1 and 2) with baseline D observing two point sources (A and B) at a wavelength λ, wavefronts from each source will arrive at the antennas at different

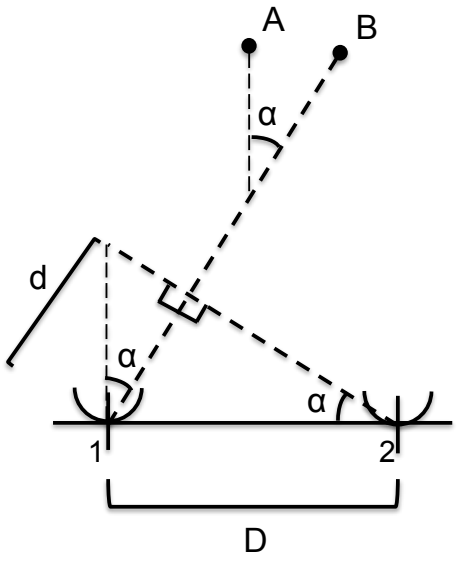

Figure 3.1: Two-telescope array observing double point source at the zenith.

times and thus with different phase. Assuming a variable electronic delay is inserted to correct for phase changes due to the Earth's rotation for source A, consider the initial case where source A is equidistant from each antenna, while source B is at an angle α relative to A, as shown in Figure 3.1. While a wavefront from source A will reach both antennas at the same time, a wavefront from source B must travel an additional distance $d = Dsin\alpha$ after reaching antenna 2 to reach antenna 1. For the wavefronts from both sources to interfere constructively, this additional distance must be an integer multiple of the wavelength, or $d = m\lambda$. Since there are two different path lengths, there are two different fringe frequencies. This combination of different frequencies results in beating. With this beat frequency, we can find the angular separation of the two point sources α. This is the fundamental component for imaging with a radio telescope array.

At a later time, when both point sources are at a lower angle (Figure 3.2), the wavefront from source A will no longer arrive at both antennas simultaneously. If source A now lies at an angle θ relative to the baseline, source B will lie at an angle $\theta - \alpha$ due to the angular difference between the sources. Thus, the additional distance traveled by wavefronts of source A between antennas 1 and 2 will be $d_A = Dcos\theta$, while that of wavefronts from source B will be $d_B = Dcos(\theta - \alpha)$. For the wavefronts to interfere constructively, the difference between the additional distances, $\Delta = d_B - d_A = D[cos(\theta - \alpha) - cos\theta]$, must be an integer multiple of the observed wavelength.

As an example, consider an antenna pair on Earth's equator with baseline 100 m observing a double source on the celestial equator with angular separation $\alpha = 1^o$ at a wavelength $\lambda = 10$ cm. When source A is at the zenith, $\theta = 90^0$, so $\Delta = 1.745$ m. When $\theta = 80^o$, $\Delta = 1.716$ m, which is a change of 2.9 cm. For constructive interference to occur, a change in Δ of 10 cm must occur, which happens when $\theta = 71^o$. Using this 19^o difference and the fact that the Earth rotates 15^o every hour, or 3600 s, the fringe period can be found using

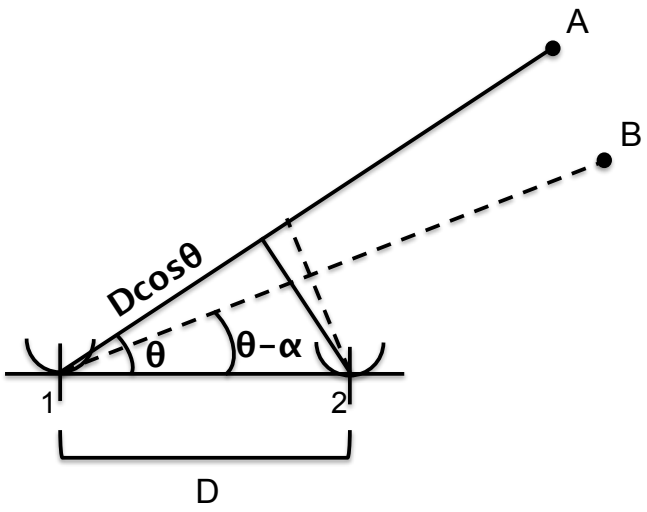

Figure 3.2: Two-antenna array observing double point source at a lower angle.

$\frac{15^o}{19^o} = \frac{3600s}{t}$, which yields $t = \frac{19^o \cdot 3600s}{15^o} = 4560s$. Inverting this to find the frequency of this cycle, $\frac{1}{4560s} = 0.22$ mHz. Thus, the observed interference pattern will undergo a cycle of fringes at a frequency of 0.22 mHz. By observing this frequency, the angular separation α can be solved for:

$$\alpha = \theta - cos^{-1}(\frac{\lambda}{D} + cos\theta) \tag{16}$$

where $\theta = 90^o - \frac{t \cdot 15^o}{3600s}$. Due to the geometry, the fringe frequency and period are not constant.

3.1.2 Fourier Imaging

For the VLBA and VLA, signals from each baseline are combined in a device called a correlator, which multiplies and time averages the signals and outputs the amplitude, phase, and frequency of the fringes, according to Burke & Graham-Smith, Ch 6.1 (2010). Because the antennas are fixed in place, the difference in arrival times, called the geometrical time delay (τ_g), can be found for a source at the "phase center" - the center of the field of view - and accounted for by the inclusion of an instrumental time delay (τ_i). This effectively "stops

the fringes" due to the Earth's rotation for a point source at the phase center. With these delays and two voltage amplitudes $x(t)$ and $y(t)$ from the antennas, the cross correlation of the amplitudes, which is similar to a convolution, can be defined as $R_{xy}(\tau) \equiv \langle x(t)y(t-\tau)\rangle$. The Fourier transform of this cross-power product can be taken to give the cross-spectrum power density, which can be used to describe the power output of the interferometer, as in Burke & Graham-Smith, Ch 3.9 (2010).

For an interferometer pair of the ith and jth elements of the array, the vector between the two elements, or the baseline vector, is $\mathbf{b}_{ij}$ or, if measured in wavelengths, $\mathbf{b}_{ij,\lambda} = \mathbf{b}_{ij}/\lambda$. The standard coordinate system for these vectors is described by (u,v,w), where w is the vector towards the source and u and v are the projected northerly and easterly directions that are perpendicular to w and each other. If the interferometer is observing an element of a source of solid angular size $d\Omega$ at frequency ν, the relative antenna area, or ratio of projected area to maximum area, will be $A(\sigma)$, where σ is the vector from the phase center to the source element; $A(\sigma)$=1 at the phase center. If the brightness of the source at ν in the direction of σ is $B_\nu(\sigma)$, the complex visibility for telescope pair (i, j), which includes the amplitude C and phase ϕ of an observation, is defined as $V_{ij} = \int A(\sigma)B_\nu(\sigma)exp(i2\pi\mathbf{b}_{ij}\cdot\sigma)d\Omega = Ce^{-i\phi}$, according to Jianjun (2007) and Burke & Graham-Smith Ch 5.3 (2010). If this equation is converted to be a function of u and v, its Fourier transform can be taken to produce the brightness as a function of right ascension α and declination δ, the orthogonal coordinates of σ in the plane of the sky, along the east-west and north-south axes, respectively.

3.2 Radio Interferometry Arrays

The two radio interferometers used were the Very Large Array (VLA) and Very Long Baseline Array (VLBA). The VLA consists of 27 steerable radio telescopes west of Socorro, New

Mexico. Each antenna is 25 meters in diameter and can move along a track, allowing the maximum telescope distance from the center of the array to range from 0.59 to 21 kilometers, according to Thompson *et al.* (1980). At a wavelength of 6 cm, the largest separation of the array allows resolution of 0.3 arcsecond. The VLBA consists of ten radio telescopes in locations ranging from Hawaii to the Virgin Islands, also with 25 m apertures. While the telescopes are fixed in place, their larger baselines allow for greater resolution (1.4 milliarcseconds at 6 cm) according to Romney (2012).

As the Earth rotates, the projected lengths of baselines change from the point of view of the observed object. Because the largest baseline can be used as long as both telescopes can observe the object, the VLA can observe for a longer duration than the VLBA, as 36 km is much smaller than the diameter of the Earth. In addition, the VLA's smaller baselines allow it to capture a very wide field of view, while the VLBA has a limited field of view. For objects at the cosmological distances that we are observing, the VLA images on kiloparsec scales, while the VLBA images on parsec scales.

3.3 Data Editing, Calibration, and Imaging

According to the editing procedure detailed in Burke & Graham-Smith (2010), the visibility data for each baseline are first examined as a function of time and frequency and bad data are "flagged," or marked so that further analysis will ignore them. Next, the data are sorted from time order to the rectilinear (u,v) coordinate system and calibrated with reference sources. Objects can be phase calibrators if they are close to the source, while flux calibrators are objects with well-known flux densities from careful monitoring programs. For three antennas i, j, and k, the sum of the three baseline phases $\phi_{ijk} = \phi_{ij}+\phi_{jk}+\phi_{ki}$, termed the closure phase, remains constant regardless of phase shifts caused by atmospheric or instrumental effects at

one telescope, as long as they are constant during integration. A related value, the closure amplitude $A_{ijkl} = \frac{V_{ij}V_{kl}}{V_{ik}V_{jl}}$ exhibits similar behavior for telescope-based amplitude errors. These quantities are used to find "complex gain" corrections (*i.e.*, phase and amplitude corrections) of all antennas for phase with respect to a single reference antenna, and for amplitude, relative to the nominal sensitivities of the antennas. With these calibrations and corrections, a model can be made and corrected iteratively by incremental adjustments of the complex gain of each antenna.

After the data are calibrated, they can be used to create a "dirty" map by calculating the Fast Fourier Transform (FFT) of the distribution of observations on the u-v plane. This map can be seen as a convolution of the brightness distribution with an imperfect beam, called the "dirty" beam, which is the response of the array to a point source. The convolution of two profiles is a measure of the shared amplitude as a function of an introduced translation in one of the profiles. At this point, the map exhibits "exaggerated" response to each element of the target source due to point source response, or spreading of brightness from a central source into a complex pattern of "sidelobes." Flux is subtracted from bright areas and added to another map of "clean components," which is initially blank. This leaves behind a residual or "difference" map. It is necessary to deconvolve the brightness from the "dirty" beam. After many iterations, when the "dirty" map no longer has discernible peaks, the clean components can be convolved with a point-spread function (the "clean" beam) to create the "clean" map. This new map can approach the theoretical thermal noise and remove the sidelobes from the point-source response, permitting a view into the deeper structure of the source. Appropriately, this method of iterative flux subtraction is called CLEAN.

3.4 Image Analysis

Both VLBA and VLA data have specific programs for cleaning and analysis. VLBA data are analyzed by the California Institute of Technology's program, Difmap, so called for the use of difference mapping, or using the result of subtracting the model of a source from a dirty map, as described by Shepherd (1997). The main functions Difmap provides are the ability to examine individual baseline data for each telescope in an array and select portions of an image to clean. By displaying the baseline data, outlying points may be excluded. Additionally, the amount of the *u-v* plane that is covered by an observation as well as the amplitude as a function of the radius from the center of the *u-v* plane can be displayed. The inclusion of a difference map allows iterative cleaning, as when areas are selected to be cleaned, the subtracted flux is accounted for in the clean components file, so additional subtractions may be done. Thus, Difmap allows inspection and cleaning of VLBI data.

VLA data are analyzed using NRAO's Astronomical Imaging Processing System (AIPS). If the input files are already cleaned, they can be stored in a map catalog and displayed for visual inspection. The maps are displayed in a greyscale contrast format and each pixel is tied to a position in a rectilinear coordinate system and a specific brightness, visible via the *curv* command and a cursor location. The units of brightness are "Janskys per beam area," where 1 Jy= 10^{-26} W/m^2/Hz and the unit of solid angle is the clean beam area. The coordinate system allows integration of brightness over a specific area, such as a rectangle (*tvbox*) or free-form shape (*tvstat*), to find flux densities in Jy. While *tvstat* allows the integration over a greater diversity of shapes, *tvbox* returns a pair of coordinates that describe the bottom left corner and top right corner of a rectangle, allowing for repeated integration over the same area. After *tvbox* returns coordinates, *imstat* may be used to integrate over the rectangle and output the highest and lowest brightness, the size in pixels,

and the integrated flux density. It is then possible to change the rectangle coordinates of *imstat* so that they describe a different rectangle, which is useful for background subtraction. One weakness of using a rectangular integration area is that if the source is extended, it must extend along the horizontal or vertical directions. If it does not, the command *lgeom* allows the map to be rotated so that the source lies along vertical or horizontal axes.

The command *slice* takes in two pixel coordinates and saves the brightness profile along the line between the two points to an output file. The data from this profile can then be extracted in the form of a table via our own Fortran code external to AIPS. The combination of the plotted profile and data points allows for identification of features and quantification of flux densities at specific points along the profile.

4 Observational Results & Analysis

4.1 Image Preparation and Feature Identification

Our sample consisted of 13 3CR lobe-dominated quasars analyzed by Bridle *et al.* (1994) and eight additional quasars from the same sample. The data for the new quasars were already cleaned and calibrated, but had not been analyzed. First, we identified central features, hot spots, and lobes of each source, and fit models to features to ascertain flux densities and sizes in order to meet the definitions of the prior work.

4.1.1 Definitions

In order to analyze both our new sample and that of Bridle *et al.* (1994), we adopted their definitions for features. The "central feature" is the region corresponding to the center of the quasar that is unresolved, implying small angular size. The "jet" is a feature that has a length/width ratio more than four, is distinct from other structures at high resolution, and is aligned with the nucleus of the parent object. These jets exhibit areas of increased emission, which are termed "knots." Because of beaming effects (*i.e.*, Doppler boosting), one jet is always more apparent than the other. This brighter jet is called the "jet," while the dimmer jet is termed the "counterjet." These jets extend until they disappear, direction of flow changes abruptly, or the flow decollimates. Areas of diffuse emission exist at the end of the jets, called "lobes." In cases where jets were not observable into the lobe emission, features that are the brightest in the lobe, have a surface brightness greater than four times that of the surrounding emission, and have a deconvolved FWHM$<$ 5% that of the largest diameter of the source are termed "hot spots." When the jet extends into the lobe, hot spots have the further requirement to be further from the nucleus than the end of the straight jet. The "straight jet" is the length of the jet that does not deviate from the initial direction

by more than one jet radius, or HWHM of the initial transverse profile. The "misalignment angle" was defined as the angle between the lines connecting the central feature and the two hot spots.

4.1.2 Images

Each of the new quasars exhibits a central feature with a one-sided jet and two lobes. Within most jets, knots are visible. For sources where data were available, vectors representing polarization are present. The orientation of these vectors represents the electric field orientation of incoming radiation, so the magnetic field in the quasar is oriented perpendicularly to the displayed vectors. The images are displayed with east-west coordinate right ascension and north-south coordinate declination. North is up and east is to the left. The central features are labeled "C" and the knots in the straight jet are labeled "K."

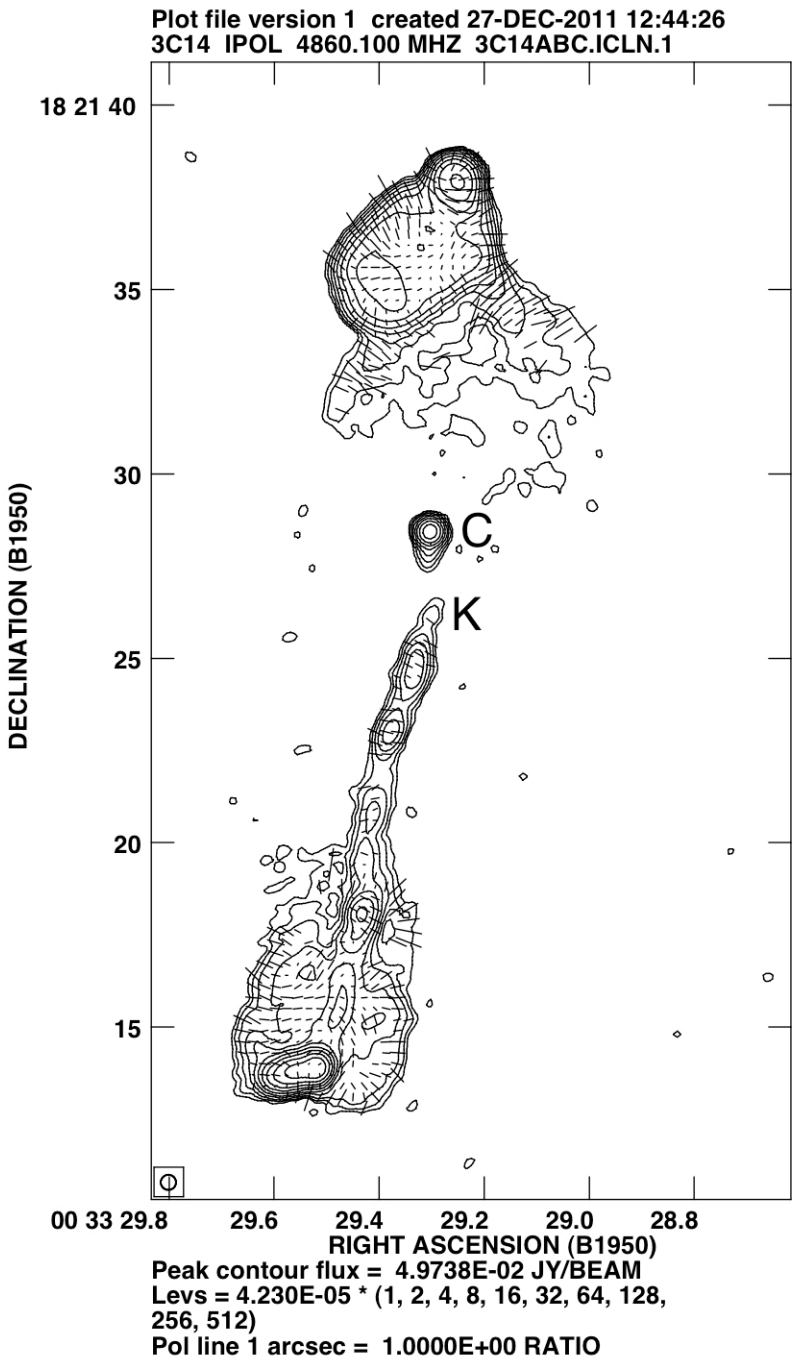

Figure 4.1: The source 3C14, where the jet extends to the southeast. The jetted hot spot is the southernmost feature in the jet, while the counterjetted hot spot is the northernmost feature in this image. The straight jet extends only to the first knot visible south of the break between the central feature and main section of the jet. The knots south of the break are all reasonably periodic and have a common elongated structure.

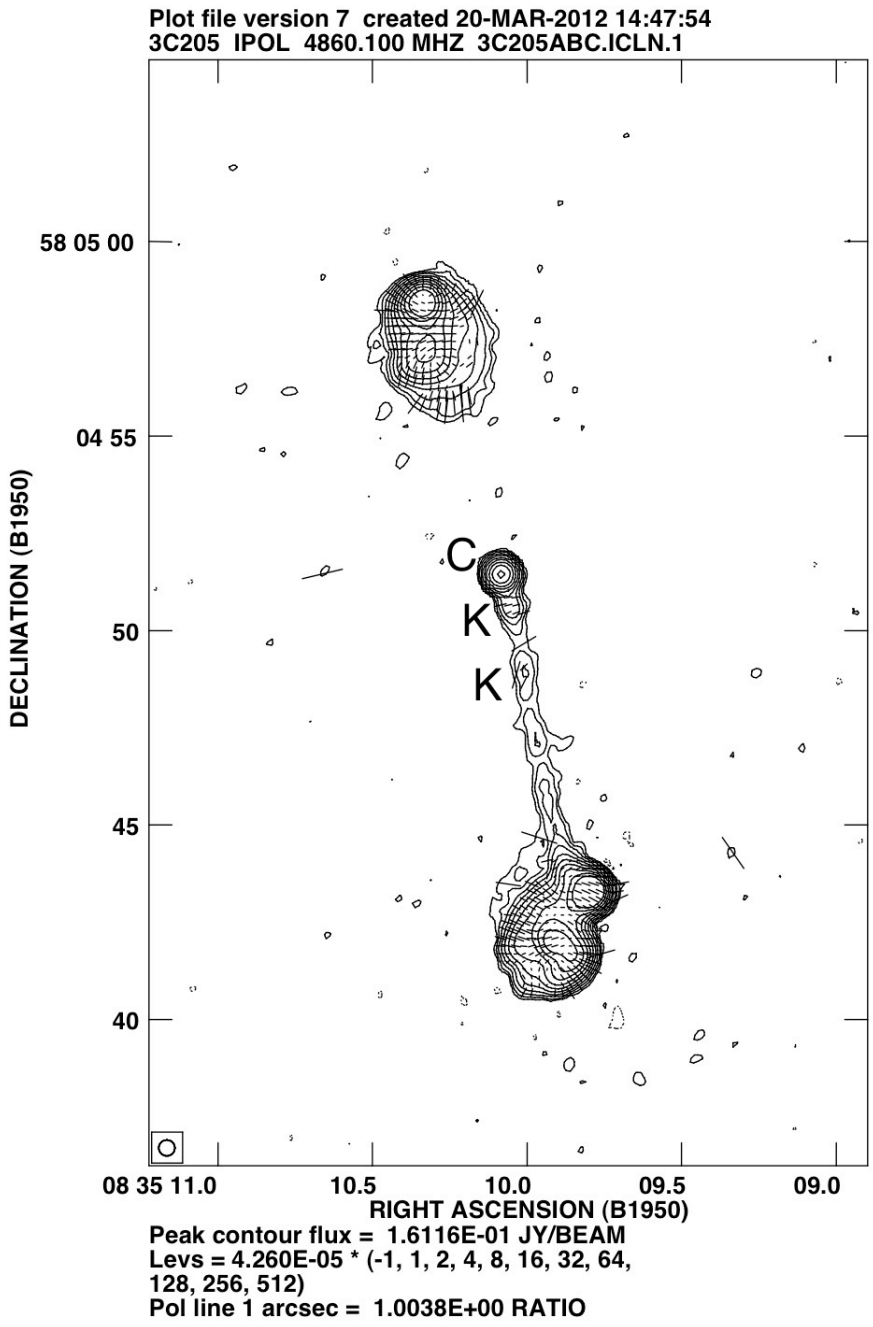

Figure 4.2: The source 3C205, where the jet extends to the southwest. The jetted hot spot is the westernmost feature in the jetted lobe, while the counterjetted hot spot is the northernmost feature in this image. The straight jet extends to the to southern border of the second knot. The shortness of the straight jet is due to an initial misalignment of the center of the central feature and the direction of the jet, so the overall jet exhibits little bending and regular, elongated knots.

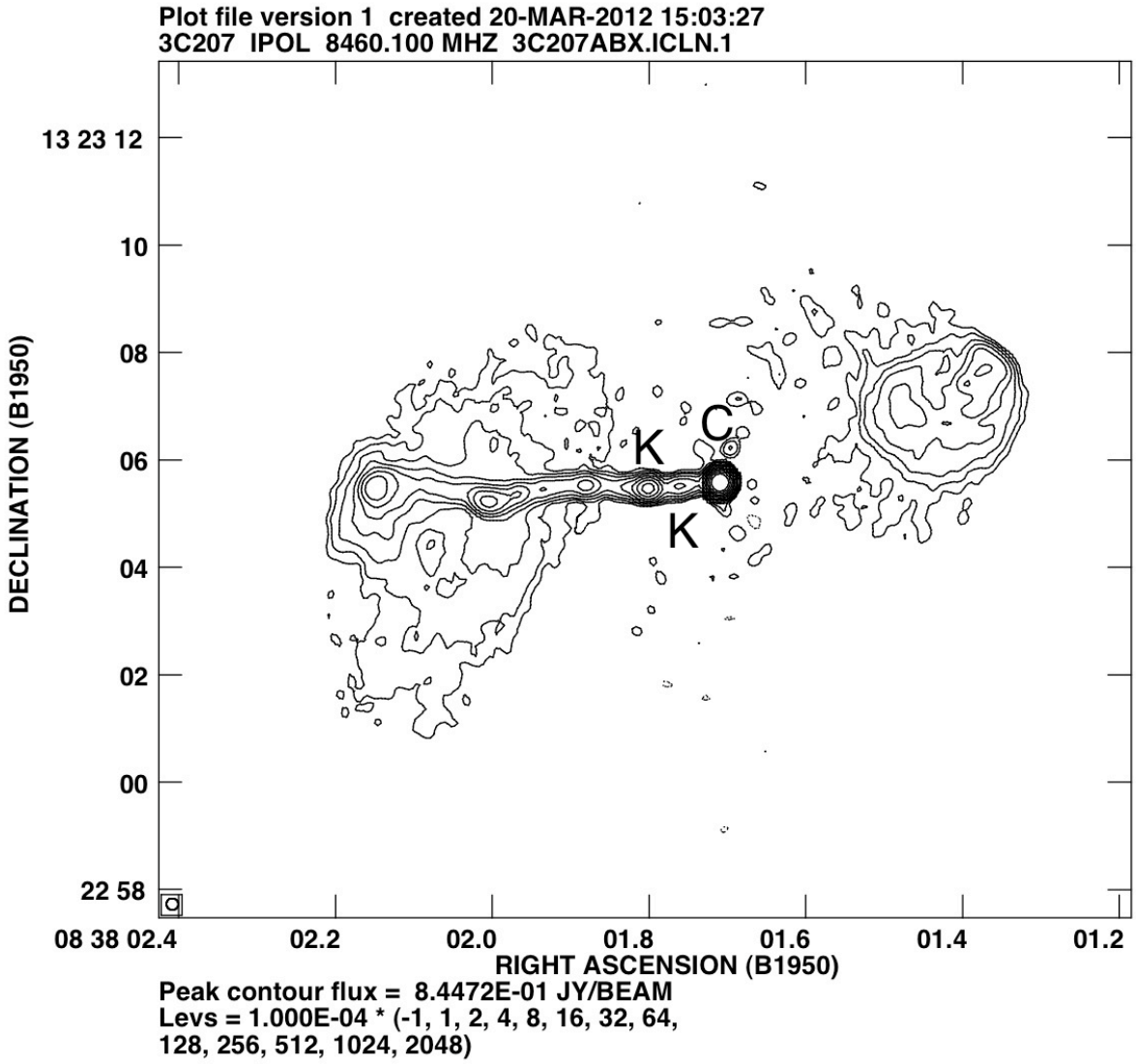

Figure 4.3: The source 3C207, where the jet extends to the east. The jetted hot spot is the easternmost feature in the jet. The straight jet extends only to the eastern border of the second knot from the central feature. Although the jet deviated from linearity, the knots were mostly regular and circular. No features in the counterjetted lobe met our hot spot requirements.

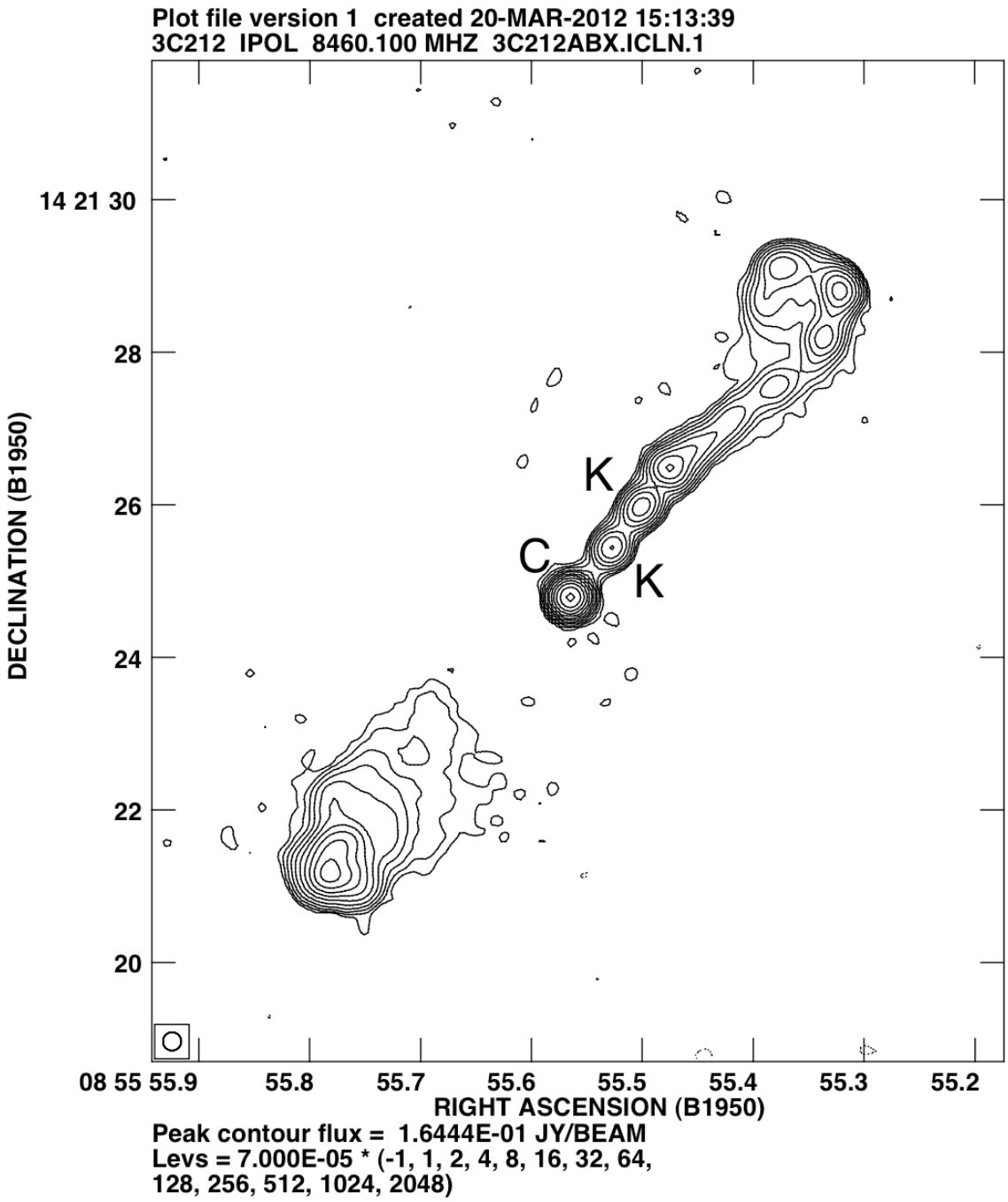

Figure 4.4: The source 3C212, where the jet extends to the northwest. The jetted hot spot is the westernmost feature in the jet. Another area of bright emission is present to the north east of the jetted hot spot, but it is not part of the jet. The straight jet extends only to the northwestern border of the second knot from the central feature. The counterjetted hot spot is the southeasternmost feature in the image.

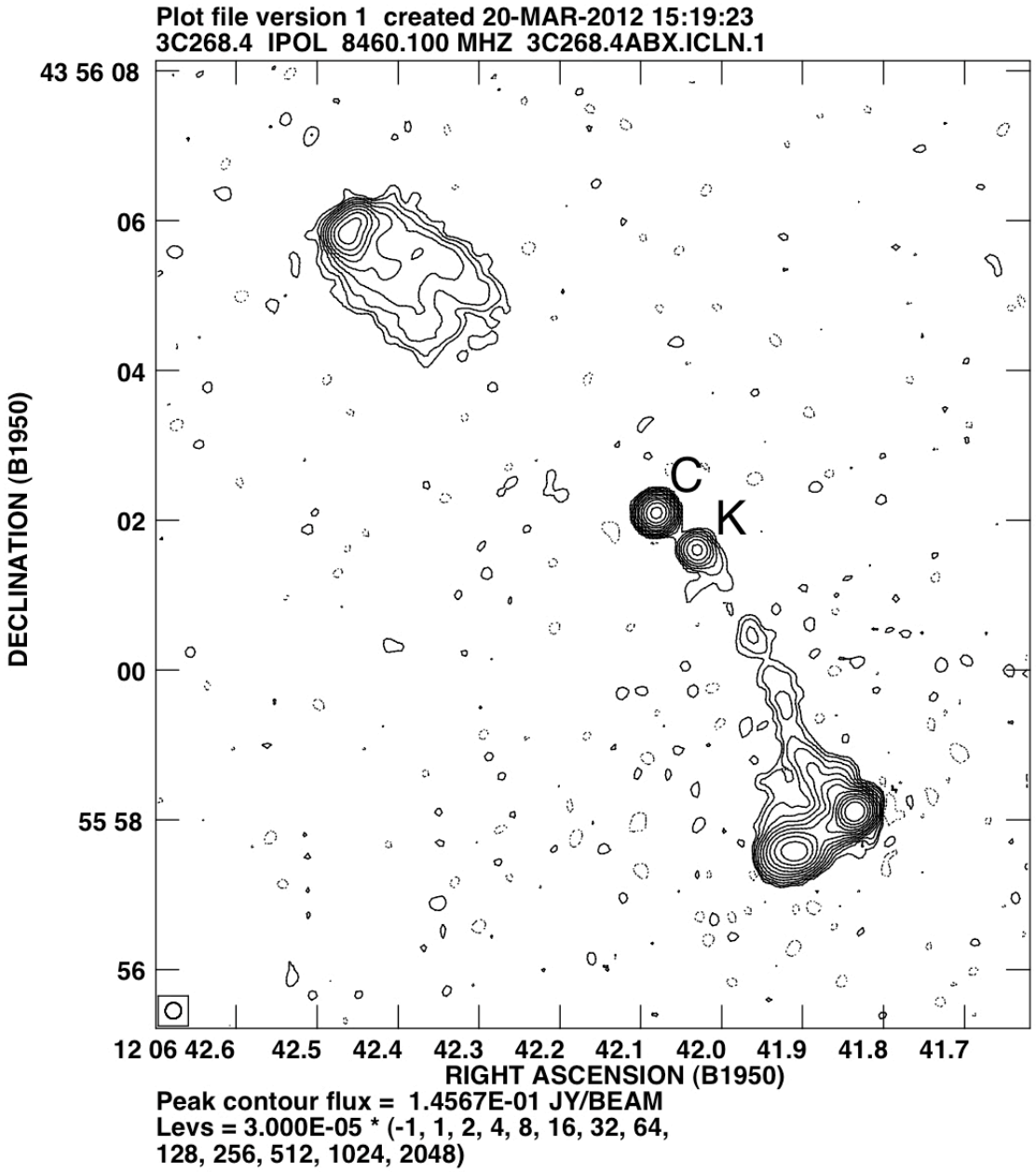

Figure 4.5: The source 3C268.4, where the jet extends to the southwest. The straight jet encompasses only the first knot southwest of the central feature. After this knot, the jet exhibits a break in emission that is accompanied by a change in direction. The jet then terminates in the jetted hot spot, which is the westernmost feature in the jet. Another area of bright emission is present to the southeast of the hot spot, but this was too far from the jet path to qualify as a hot spot. The counterjetted hot spot is the area of high emission to the northeast.

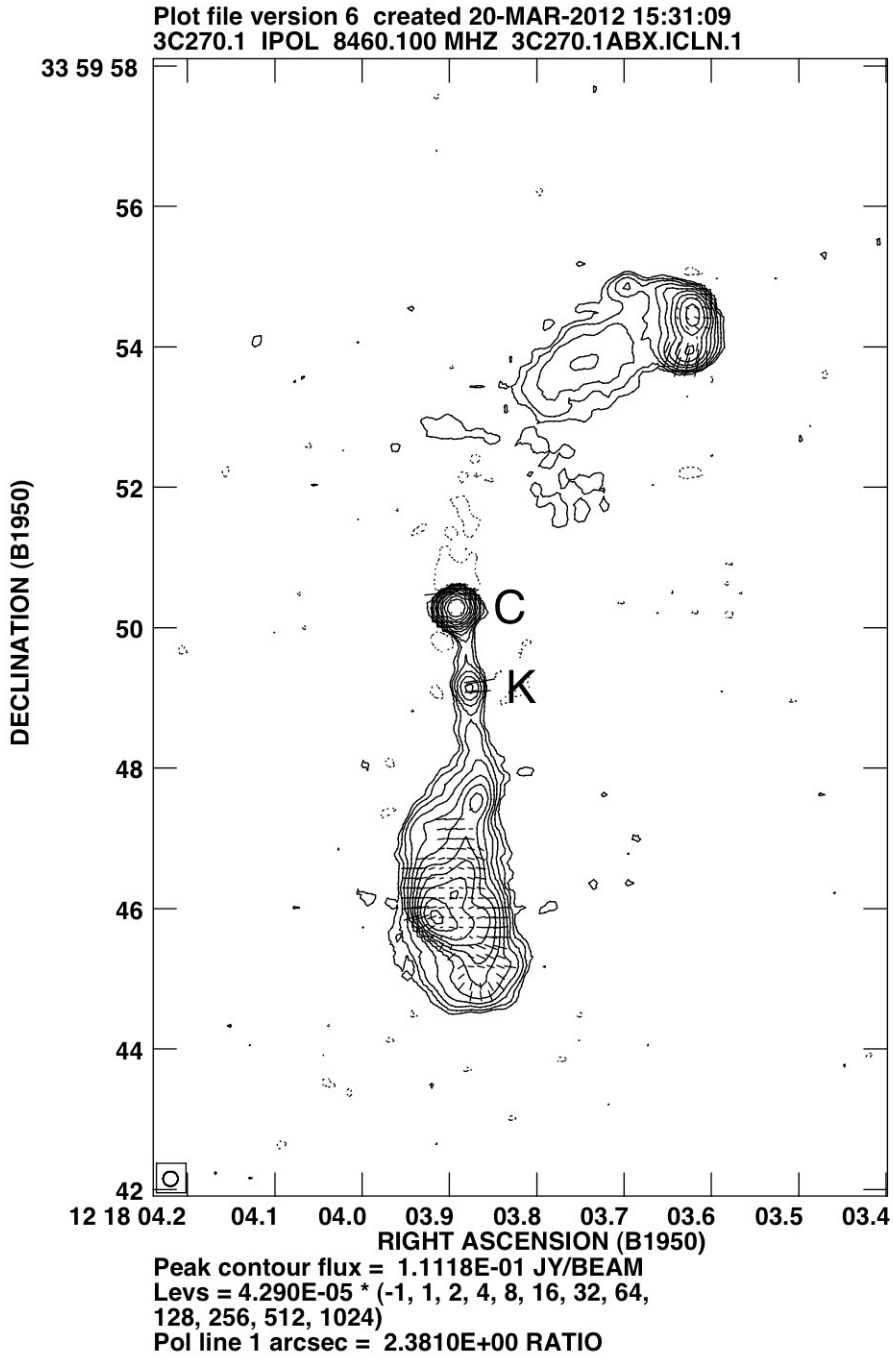

Figure 4.6: The source 3C270.1, where the jet extends to the south. The jetted hot spot is the southernmost feature in the lobe. The straight jet extends only to the southern border of the first knot from the central feature. The counterjetted hot spot is the highest area of emission to the north of the central feature. Note that the dashed contours north of the central feature signify negative flux, a sign of minor cleaning errors.

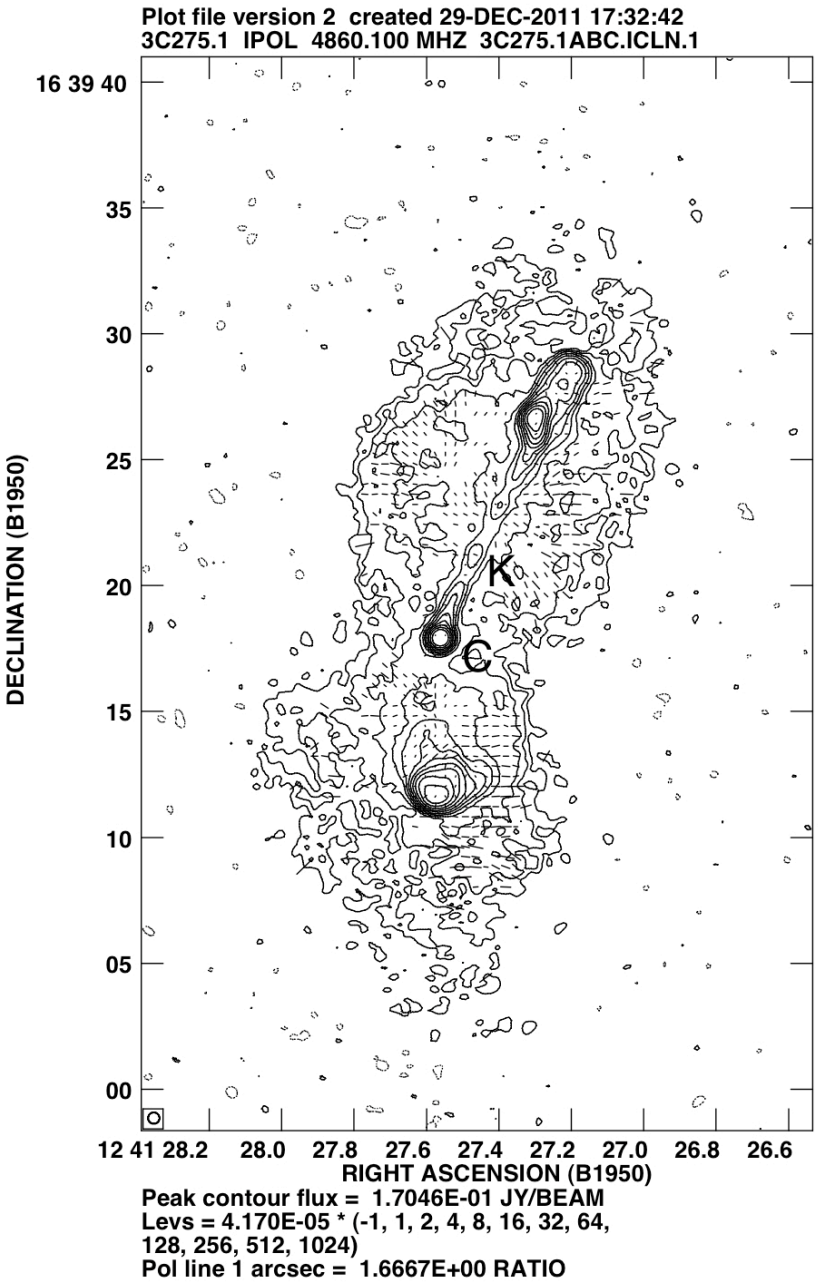

Figure 4.7: The source 3C275.1, where the jet extends to the northwest. Moving north along the jet from the central feature, a region of decreasing emission that is not compact enough to be termed a knot is encountered. The straight jet encompasses only this region and the following knot. After this feature and two knots, the jet terminates in the hot spot, after which there is an area of peaked emission. The counterjetted hot spot is the area of high emission to the south of the central feature. Although the source is surrounded by an area of considerable emission, all features stood out above this base level.

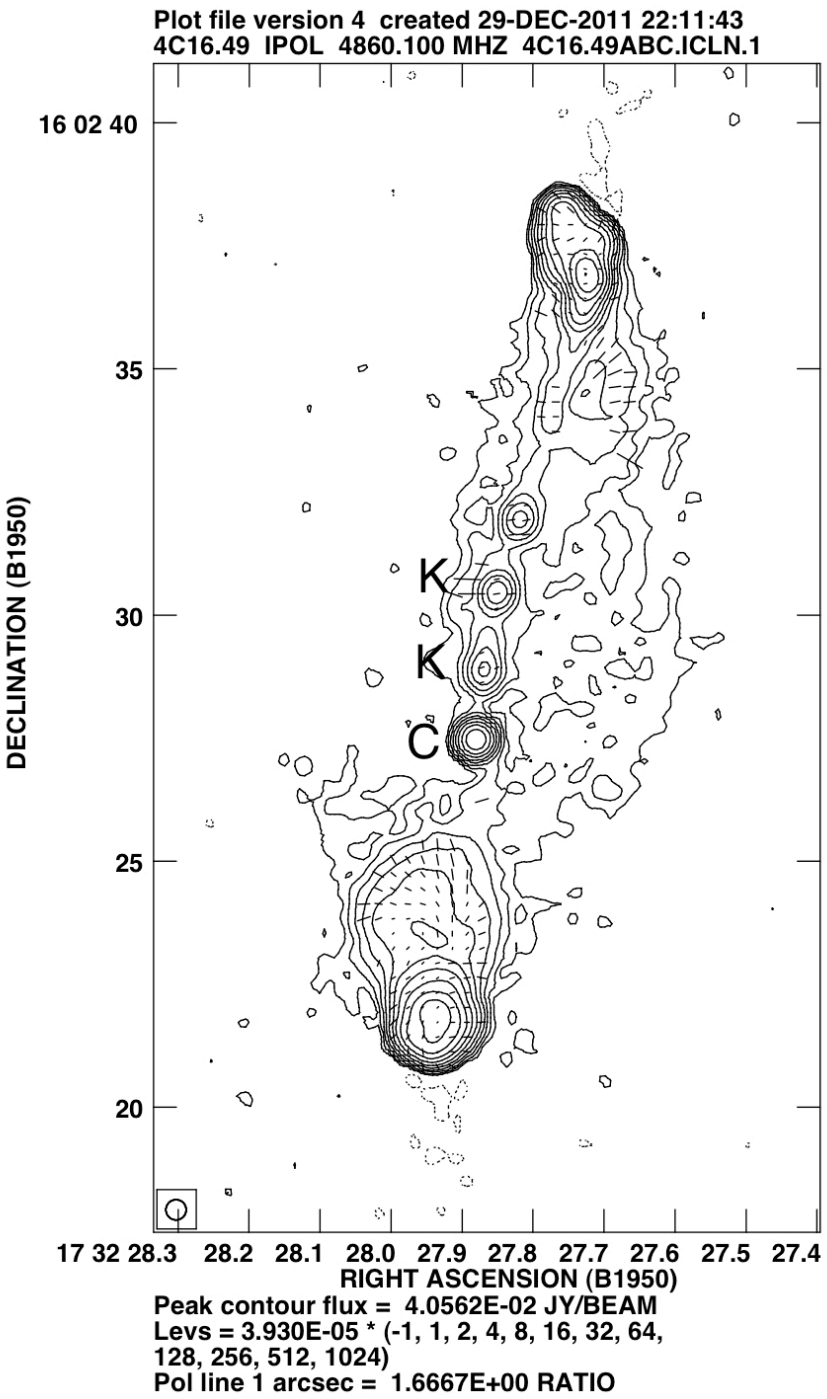

Figure 4.8: The source 4C16.49, where the jet extends to the north. After three knots, the jet terminates in the hot spot, which is the northernmost feature in this image. The straight jet ends between the second and third knots. The counterjetted hot spot is the bright feature to the south of the central feature.

4.2 Small- & Large-Scale Kinematics

In order to relate the kinematics of the small-scale jet to the kiloparsec scale, the prominences of the jet and the central region with respect to extended emission from the jetted lobe, the counterjetted lobe, and the combined lobes were analyzed. Here, prominences are defined as the ratio of feature flux to extended flux at a rest-frame frequency of 5 GHz. The relationship between these two prominences was a key, but tentative, result from Bridle *et al.* (1994) that we examined with a larger number of sources.

Because VLA images have lower resolution, they have a higher flux density for the central feature than VLBA images. In order to take this flux into account when distinguishing between central feature and jet flux, the following analyses on two data samples were performed: one where the difference between the flux density between the two resolutions (the intermediate flux) was assigned to the central feature (A) and the other where it was assigned to the jet (B).

In Figure 4.9, the slope above the legend corresponds to that of the correlation for sources with intermediate flux added to the central feature (A condition), while the slope below the legend corresponds to the B condition. Although all of these correlations are highly significant, the B condition with the jetted lobe as the extended source gave the best fit (confidence level $> 99.9\%$). In order to test if any other source properties are strongly influencing the prominence correlation, we subdivided the sample according to source properties and examined the distribution of sources within the prominence plot.

One of the properties used to divide the sample was the hot spot recession ratio, which is the ratio of the distance between a hot spot and the central feature to the lobe extent. Here, the lobe extent was defined as the furthest distance from the central feature that extended lobe emission was more than twice the image noise. Figure 4.10 shows the distribution

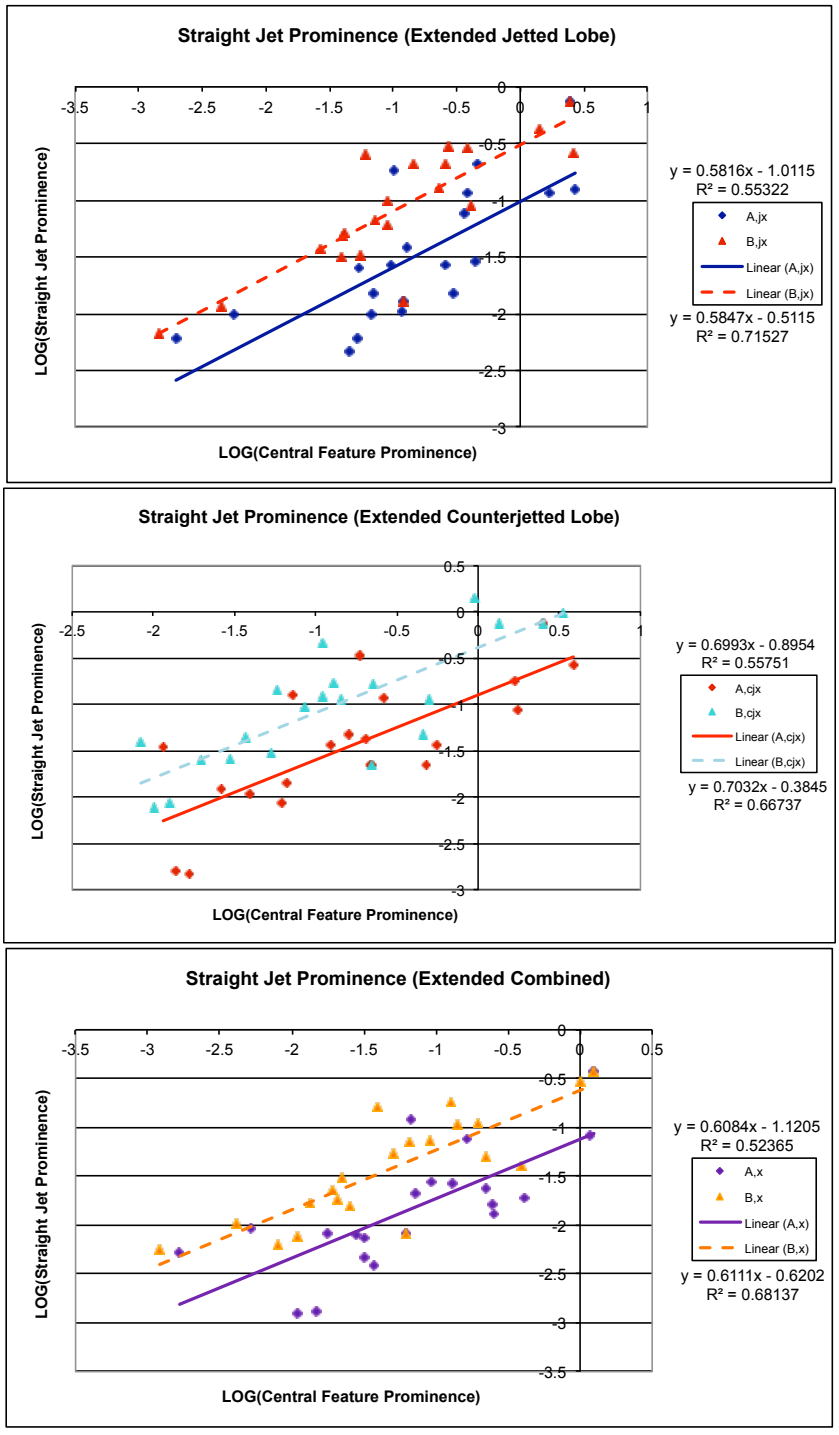

Figure 4.9: Straight jet prominence vs. central feature prominence for three different normalizations by extended emission.

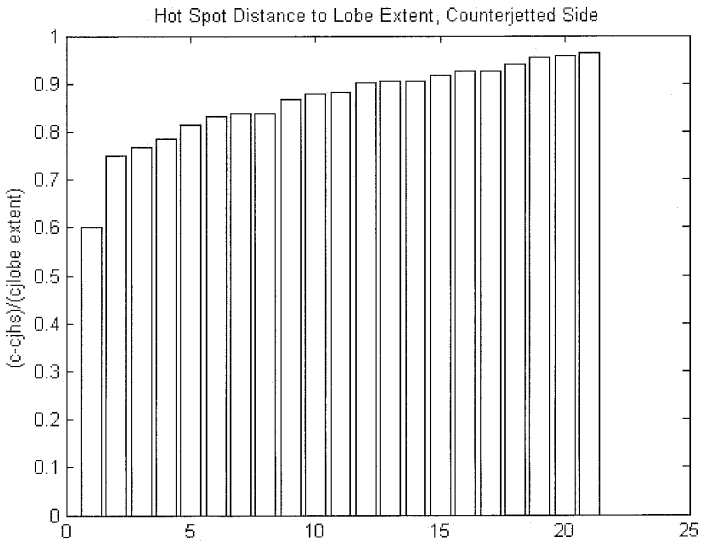

Figure 4.10: Distribution of counterjetted hot spot recession ratios for sample.

of counterjetted hot spot recession ratios in our sample. There is an even distribution between approximately 0.75 and 0.95, but the smallest source (3C275.1) is unusually small. Because of this, the sample was divided into almost equal sections between those above and below 0.88. Figure 4.11 shows the straight jet/central feature prominence relation for the sample divided into these sections. Both the high and low recession ratio subdivisions are well mixed and do not affect the correlation, although the high ratio sources return a higher correlation.

Similarly, Figures 4.12 and 4.13 show the source distribution and prominence relation for subsamples separated according to jetted hot spot recession ratios. The ten sources with the highest ratios are similar, but the distribution at smaller ratio values begins to decline until the source with the smallest ratio (3C215), which is much smaller than the previous changes in ratio would suggest. Both subsamples are well mixed and maintain the correlation.

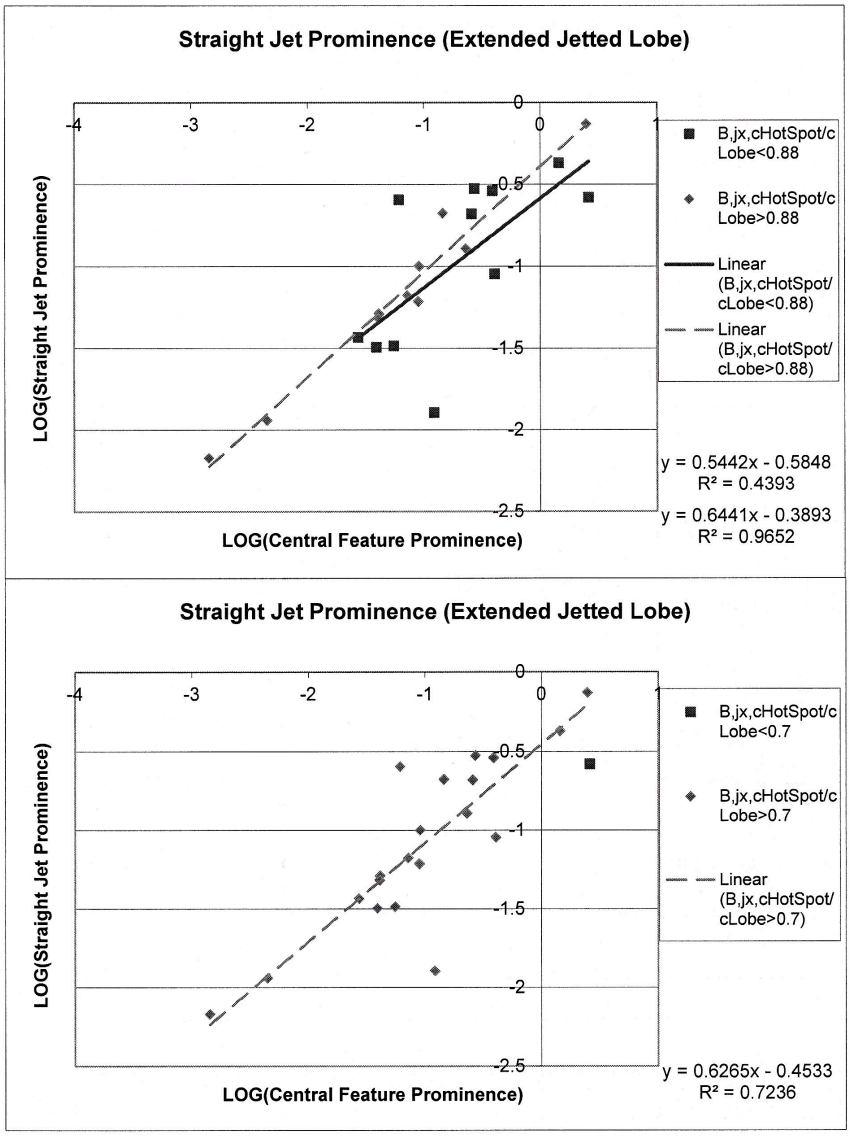

Figure 4.11: Straight jet prominence vs. central feature prominence normalized by jetted lobe emission, subdivided for counterjetted hot spot recession ratio. In the lower plot, the single square is 3C275.1.

In addition to hot spot recession ratios, the subsamples were separated according to the following ratio: the distance from the central feature to the jetted hot spot divided by the distance from the central feature to the counterjetted hot spot. Figures 4.14 and 4.15 display

Figure 4.12: Distribution of jetted hot spot recession ratios for sample.

the ratio distribution and correlation plots. Because the seven sources with the highest ratios were quite different than the rest of the sample, the sample was subdivided into the upper seven sources and the lower fourteen. Both subsamples were well mixed and maintained the correlation.

The sample separated according to the ratio of the jetted lobe extent to the counterjetted lobe extent was then examined, with the ratio distribution and correlation plotted in Figures 4.16 and 4.17. The sample was subdivided into the highest eight sources and the lower thirteen because of the gap between them. Both subsamples are well mixed and maintain the correlation, although sources with a small ratio returned a better fit.

The data had a redshift range of 0.3 to 2, so the prominence correlation divided according to source redshift was examined. The redshift distribution and prominence correlation are shown in Figures 4.18 and 4.19. Both subsamples are well mixed and maintain the correlation.

In order to explore the relationship between misalignment angle and jet kinematics, the

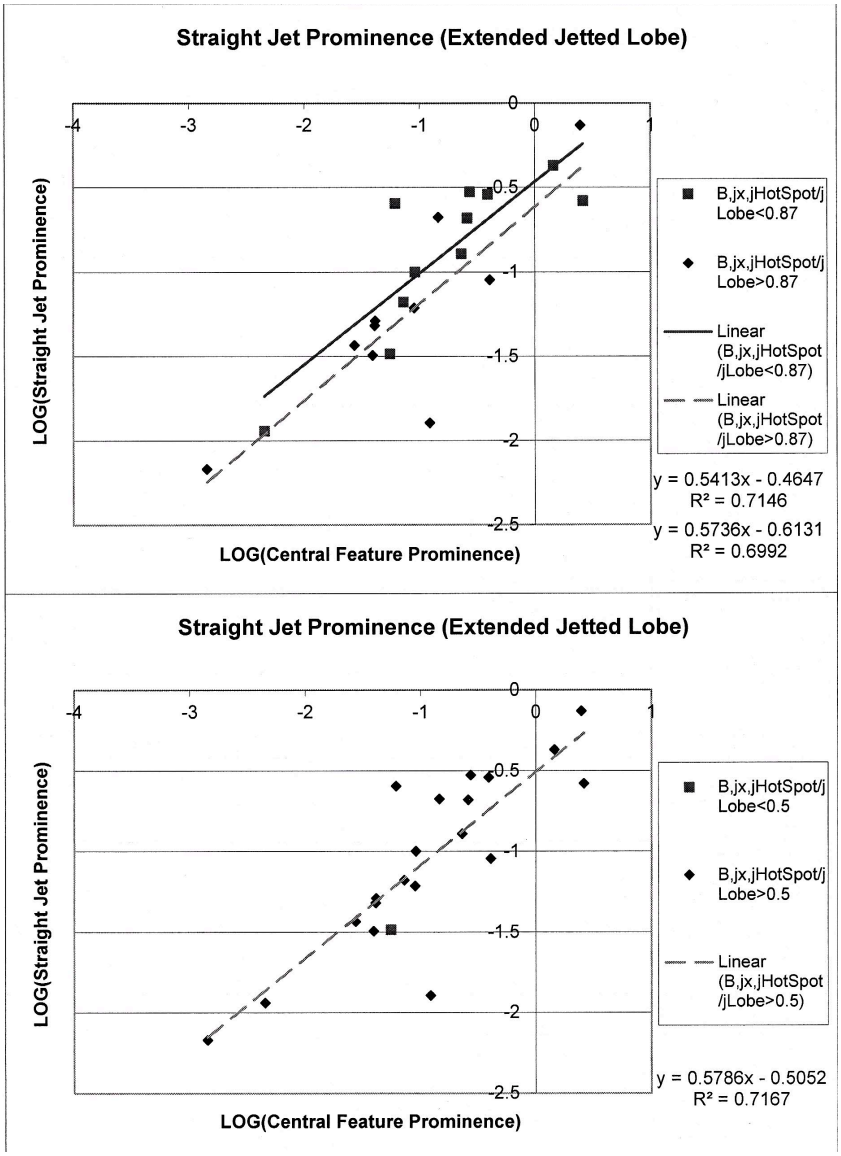

Figure 4.13: Straight jet prominence vs. central feature prominence normalized by jetted lobe emission, subdivided for jetted hot spot recession ratio. In the lower plot, the single square is 3C215.

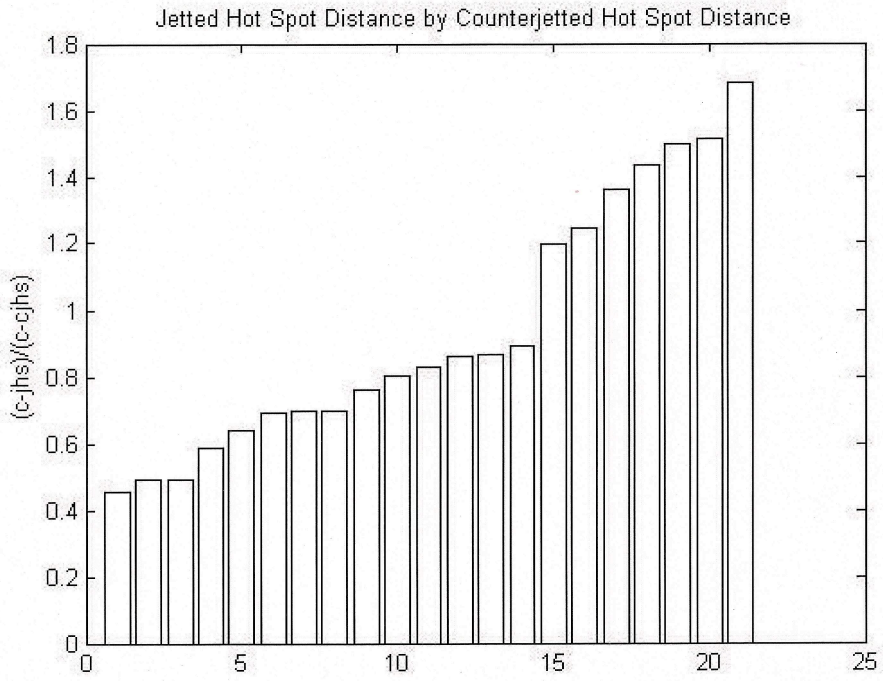

Figure 4.14: Distribution of hot spot distance ratios for sample.

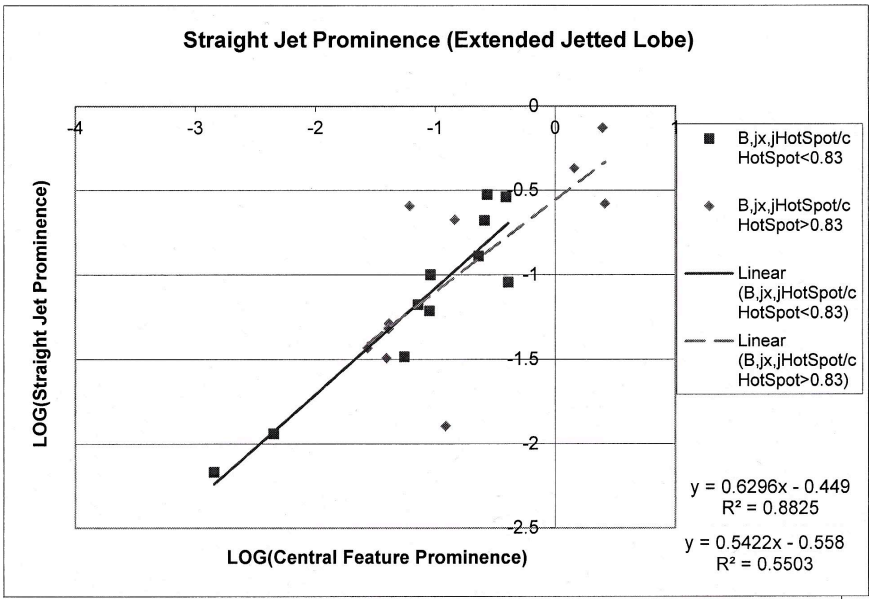

Figure 4.15: Straight jet prominence vs. central feature prominence normalized by jetted lobe emission, subdivided for hot spot distance ratio.

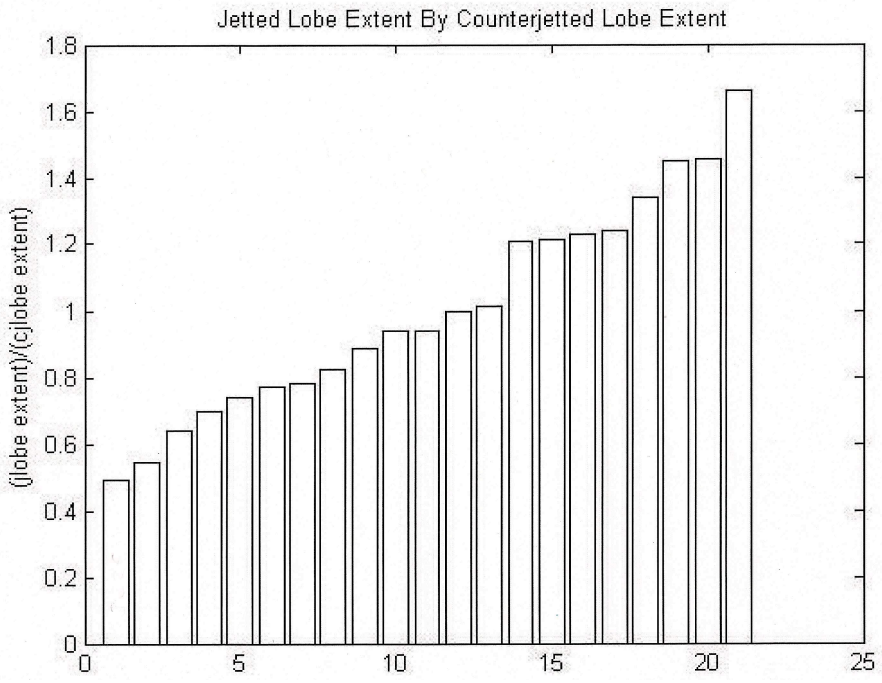

Figure 4.16: Distribution of lobe extent ratios for sample.

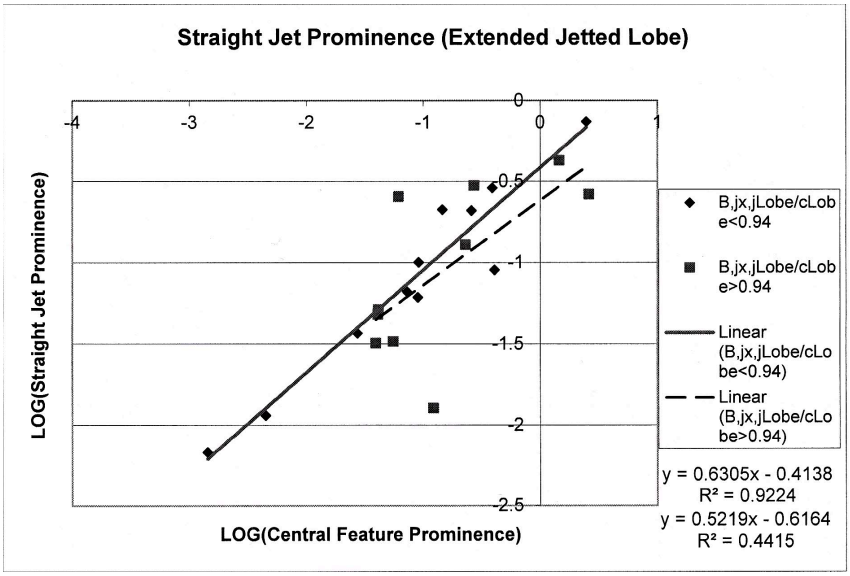

Figure 4.17: Straight jet prominence vs. central feature prominence normalized by jetted lobe emission, subdivided for lobe extent ratio.

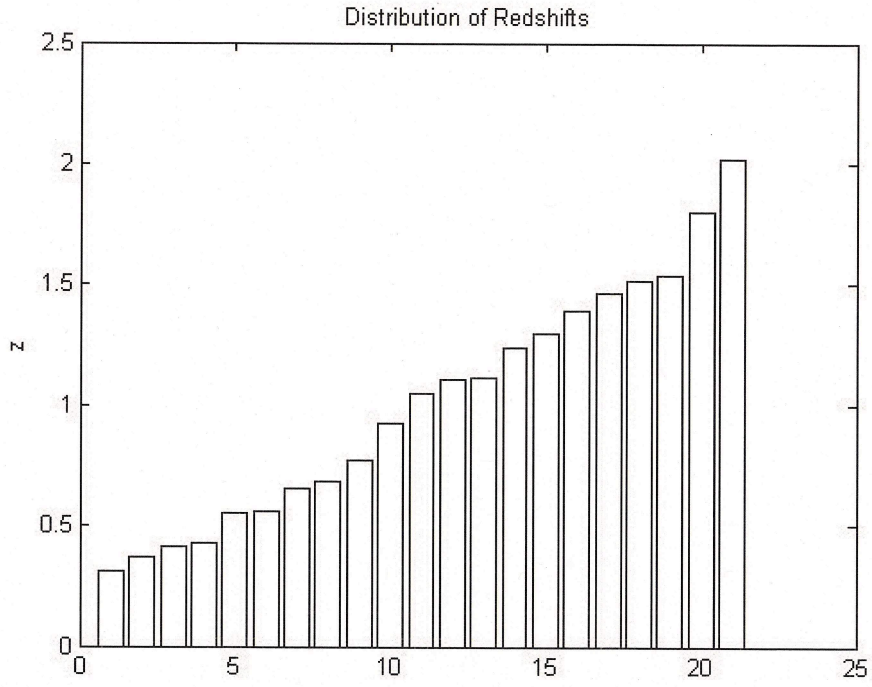

Figure 4.18: Distribution of redshifts for sample.

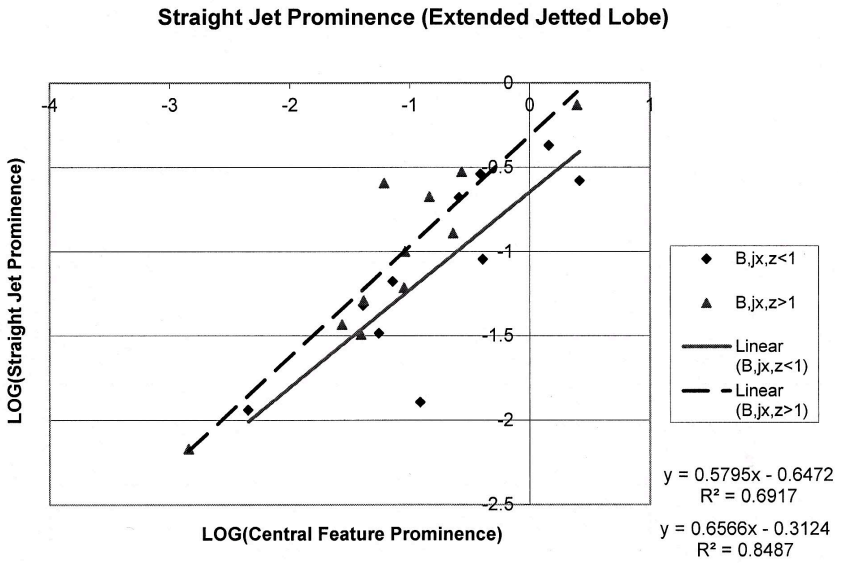

Figure 4.19: Straight jet prominence vs. central feature prominence normalized by jetted lobe emission, subdivided according to redshift.

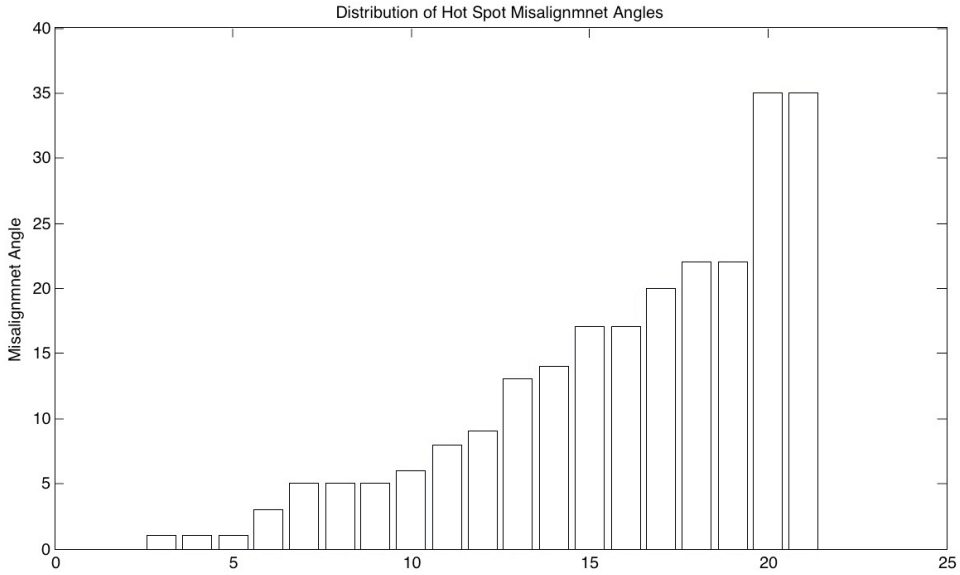

Figure 4.20: Distribution of misalignment angles for sample.

prominence relation divided according to misalignment angle was examined. There is a wide range of values, as seen in Figure 4.20, so the sample was split into ten sources with low values and eleven with high values. Note that two sources had misalignment angles of zero. Figure 4.21 shows that both subsamples are well mixed and maintain the correlation.

While some sources exhibited a series of coherent knots, such as 3C334, others had less regular knots, such as 3C268.4. In order to determine if the existence of knot trains affects the prominence correlation, the sample was divided into those with knot trains and those without (Figure 4.22). Both subsamples are well mixed and maintain the correlation.

Because only seven of the samples in our source exhibited counterjet candidates, the sample was divided into sources with counterjet candidates and those without. Figure 4.23 shows the prominence correlation for this division. Both subsamples are well mixed and maintain the correlation, although sources with counterjet candidates have a much tighter fit.

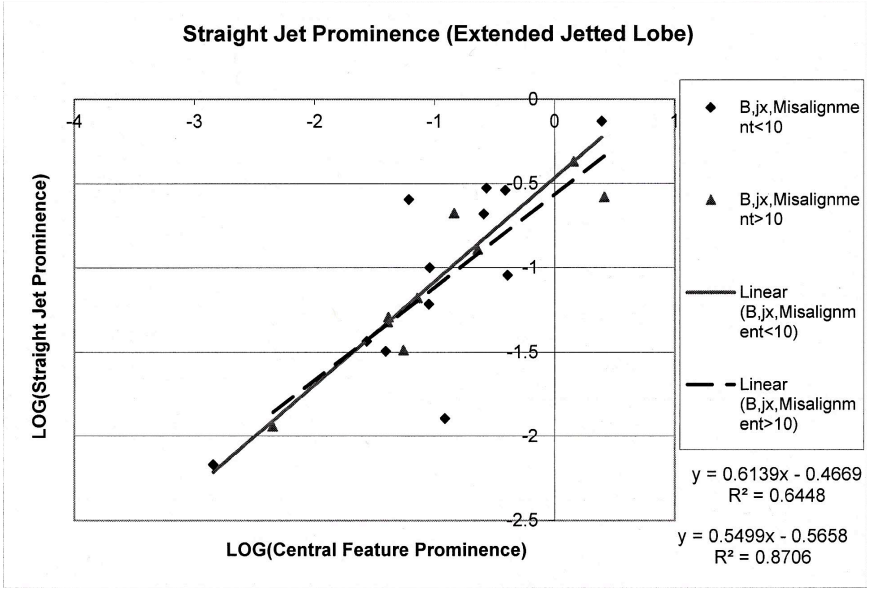

Figure 4.21: Straight jet prominence vs. central feature prominence as functions of jetted lobe emission, subdivided according to misalignment angle.

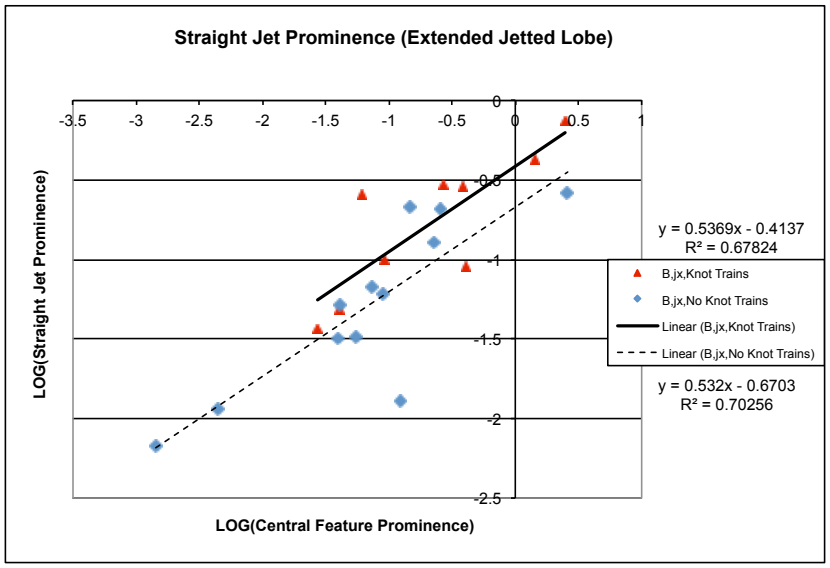

Figure 4.22: Straight jet prominence vs. central feature prominence as functions of jetted lobe emission, subdivided according to presence of knot trains.

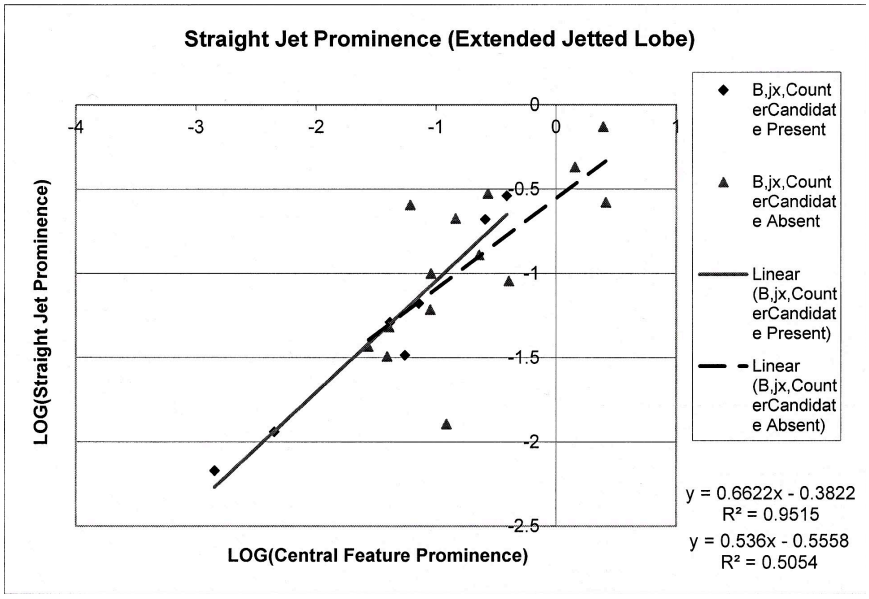

Figure 4.23: Straight jet prominence vs. central feature prominence normalized by jetted lobe emission, subdivided for counterjet candidate detection.

4.3 Jet Bending

Figure 4.24 depicts three measures of jet bending. They are defined by "position angles" of lines connecting the central feature, which is represented by black circles, to knots, which are white circles, or to the hot spot, which are represented by hatched circles. The position angle is 0^o to the north. On the left (η_{1C}), the lines connect the central feature to the first knot and to the hot spot, as a measure of initial vs. final jet direction. In the center (η_{2C}), the lines are drawn through the smallest and largest position angles, as a measure of maximum side-to-side jet bending. On the right (η_{3C}), the lines are drawn through the two consecutive features with the largest position angle difference, as a measure of maximum local jet bending.

Using these angle definitions, the correlation between hot spot strength and angle of jet bending was tested. It was theorized that jet bending would dissipate energy that would

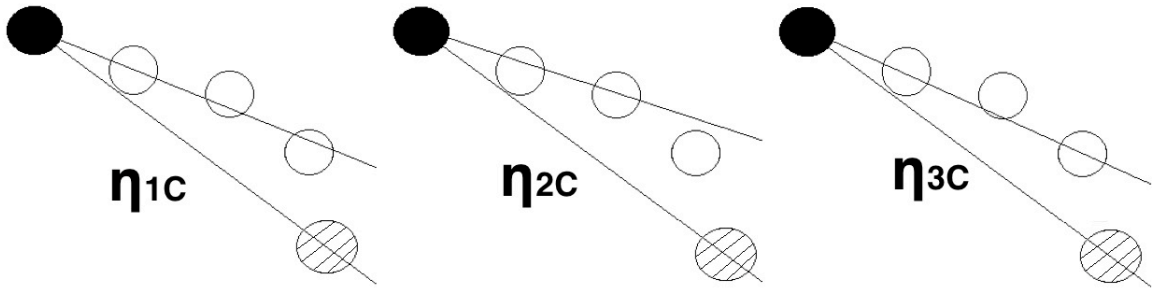

Figure 4.24: Definitions of jet bending.

otherwise be delivered to the hot spot, in which case a straight jet would have a stronger hot spot. The results for the hot spot prominence-bend angle correlation tests are given in Figure 4.25.

These anticorrelations are significant at the $98-99\%$ confidence level, but are all dependent on a small number of sources, with η_{3C} obviously relying on a single source with bizarre morphology (3C215). Even the best case of η_{2C} drops to below 90% confidence level with the omission of 3C215.

Because this relationship was reliant on a single source, we conclude that this fragile correlation found in Bridle *et al.* (1994) is not supported by our own analyses.

Because η_{2C} returned the best fit, this angle was used in tests dividing the sample by various source properties. In order to test the reliance of this relationship on various source parameters, we subdivided the sample according to source properties and examined the distribution of sources within the plot of hot spot prominence as a function of bend angle. The sources with the highest values of η_{2C} showed no preference for any source properties, so no dependences were found.

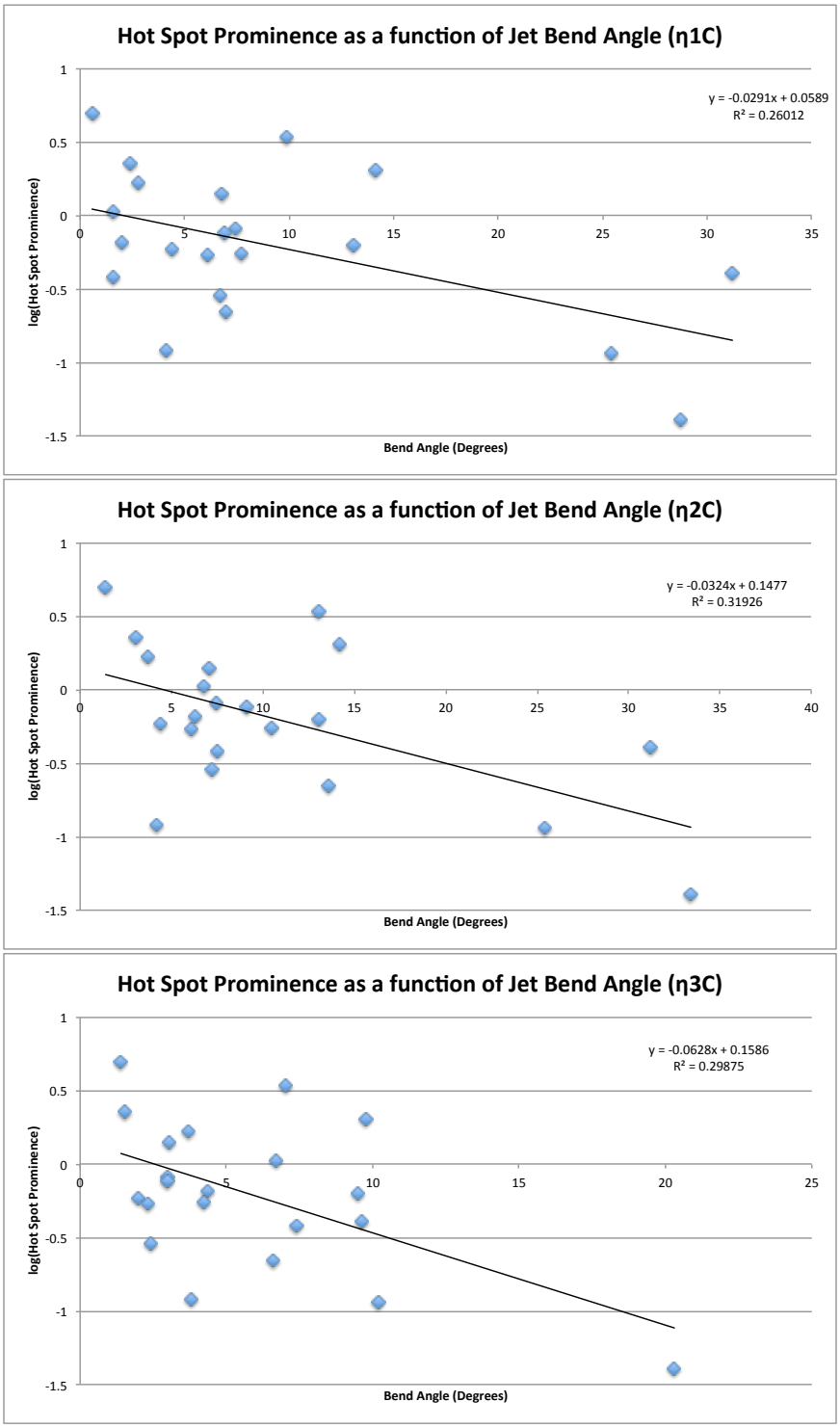

Figure 4.25: Hot spot strength as a function of bend angle.

4.4 Interknot Emission

The knots are disturbances in the flow of the jet, so it was thought that by isolating the emission between knots, the underlying flow could be determined. First, a slice along the jet was taken for the sources 3C263 and 3C334, as shown in Figures 4.26 and 4.27.

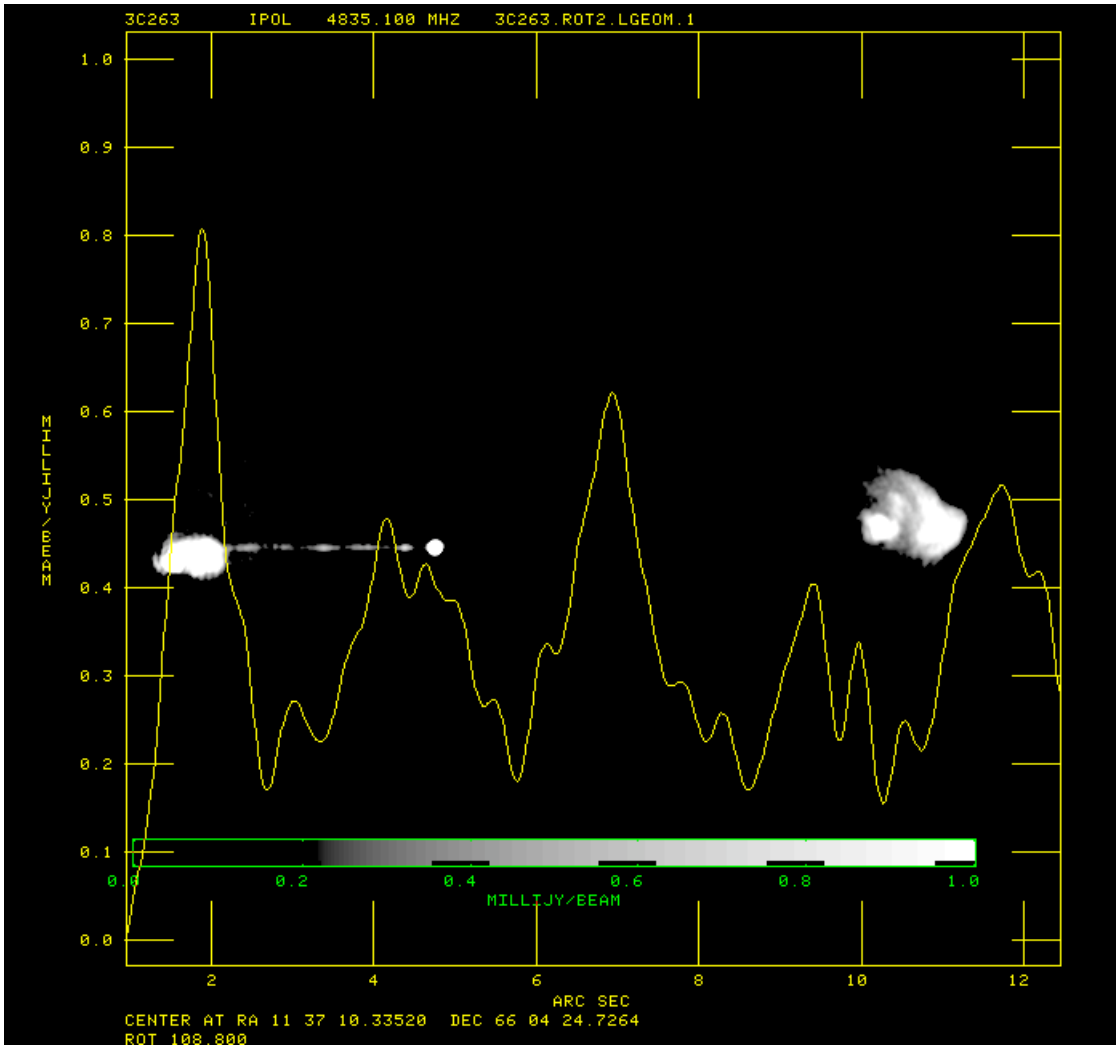

Figure 4.26: A longitudinal slice along the central ridge of the jet of 3C263. An image of the source is present in the background. The slice includes all knots between the central feature and the jetted lobe.

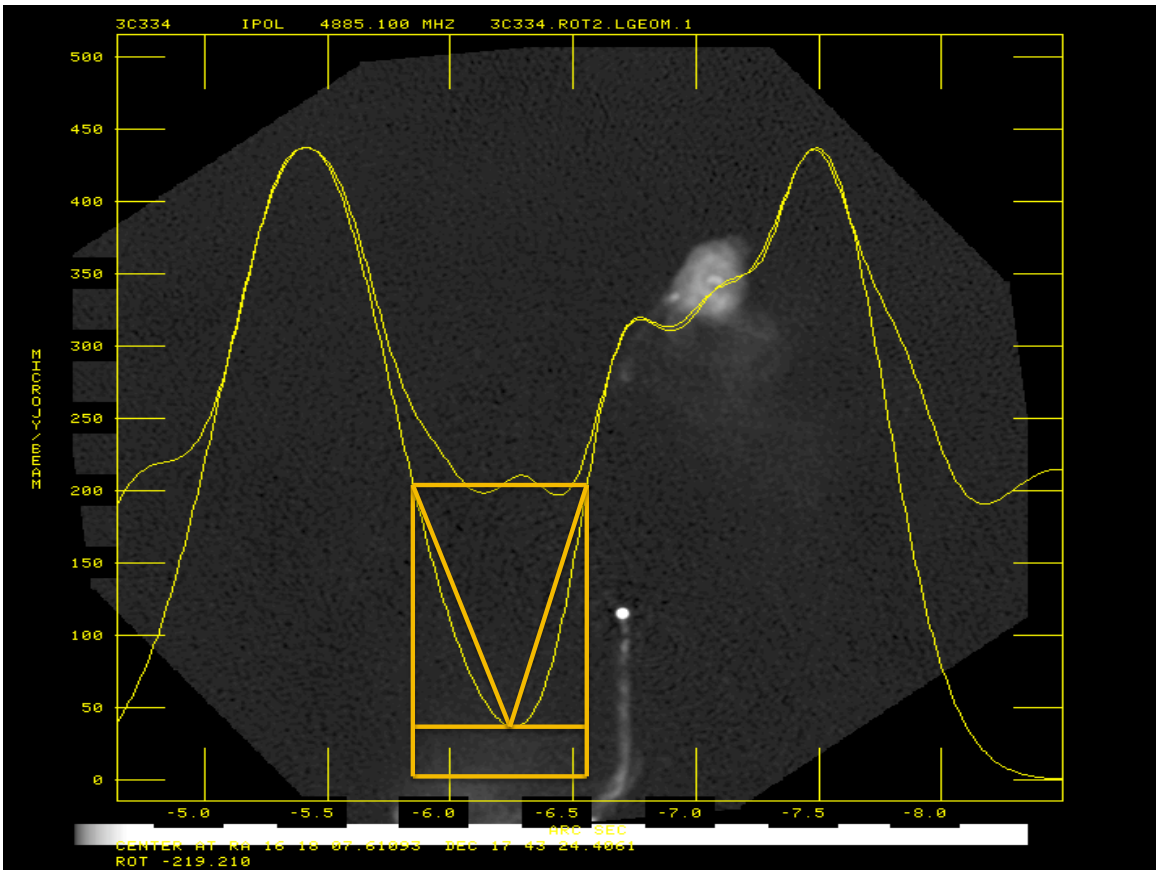

Figure 4.27: Two knot complexes of 3C334 fitted with four Gaussian components. The triangles and rectangle represent areas of background subtraction.

Then each knot complex on either side of the interknot region was fitted with a maximum of four Gaussian models of variable width and amplitude. The top of the interknot region was determined by averaging the values within the region, while the bottom of the region was the point at which the combined Gaussians were lowest. The contributions of the Gaussian components were approximated as triangles with vertices at the edges of the top of the region and at the center of the bottom. The bottom rectangle was defined by the bottom line and the zero level line.

Next, four levels of background subtraction were adopted as follows:

1. Subtract Gaussian approximation triangles and bottom rectangle
2. Subtract Gaussian approximation triangles
3. Subtract $\frac{1}{2}$ level 1
4. Subtract $\frac{1}{2}$ level 2

The first two levels give lower limits on interknot emission by subtracting the maximum possible background. The last two levels give higher estimates, which are most likely better estimates, as the background contribution of the knot complexes approaches zero at the edge of the jet.

For each level of background subtraction, the pixel values at the edges of the bottom rectangle were found and *imstat* was used to integrate over an area with the width of the jet and the length of the determined interknot region. The resulting flux densities were used to find the percentage of total jet flux contained in the interknot regions.

Because this method tended to depend on subjective criteria to define an interknot region, another method dependent on the value of knot peaks relative to interknot minima was adopted. The rules of this method were:

1. Features more than 50% of the knot peak above the minima on each side belong to the "knot complex." This includes well-resolved features and inflection points ("shoulders").

2. The half width of a knot complex is defined by the lower of the 10% levels on either side, symmetrically extended toward the higher side to yield the full width at 10%.

3. The "interknot region" is initially defined as the zone between the 10% levels of

adjacent knot complexes. Exceptions are then made (a) using the knot complex border from (1.) when this minimizes the inter-knot region and (b) using the lower 10% level for two simple Gaussian peaks.

These rules do not purport to yield physical knot vs. inter-knot zones with precision, but they are useful for trying to distinguish these two zones. Minor errors may have been made in the application of these rules, but their simplicity limits these errors to only a few percent.

These rules were applied to a larger sample of nine sources, and the resulting interknot regions were classified. If they were directly before the first major knot peak, they were placed in the first region. Some "candidate" interknot regions before the first region were not included in our analyses because they were undefined using our criteria. The later interknot regions were numbered sequentially.

For the case of 3C334 (shown in Figure 4.28), the region between knot F and knot G is interknot region 1, region 2 is between G and I, etc. Additionally, G is knot 1, I is knot 2, etc.

In order to quantify the relationship between the knot and interknot strength, the prominences of the interknot and knot regions with respect to the jetted lobe for each source were calculated. These are plotted in Figure 4.29 vs. the central feature prominence. The R^2 value of each fit corresponds to a error in the slope (m) of $0.40m$ and $0.36m$ for the interknot and knot prominences, respectively. Thus, the slopes were 0.77 ± 0.31 and 0.98 ± 0.35, so they are both $\geq 2.5\sigma$ and thus the correlations are significant at the $96 - 97\%$ confidence level. Additionally, the slopes agree to within one standard deviation. This is the first time that knot and interknot emission has been shown to be independently beamed.

To look at the possible change in beaming parameters along the jet as communicated by knot or interknot flux changes, the nine-source average and standard deviation of the

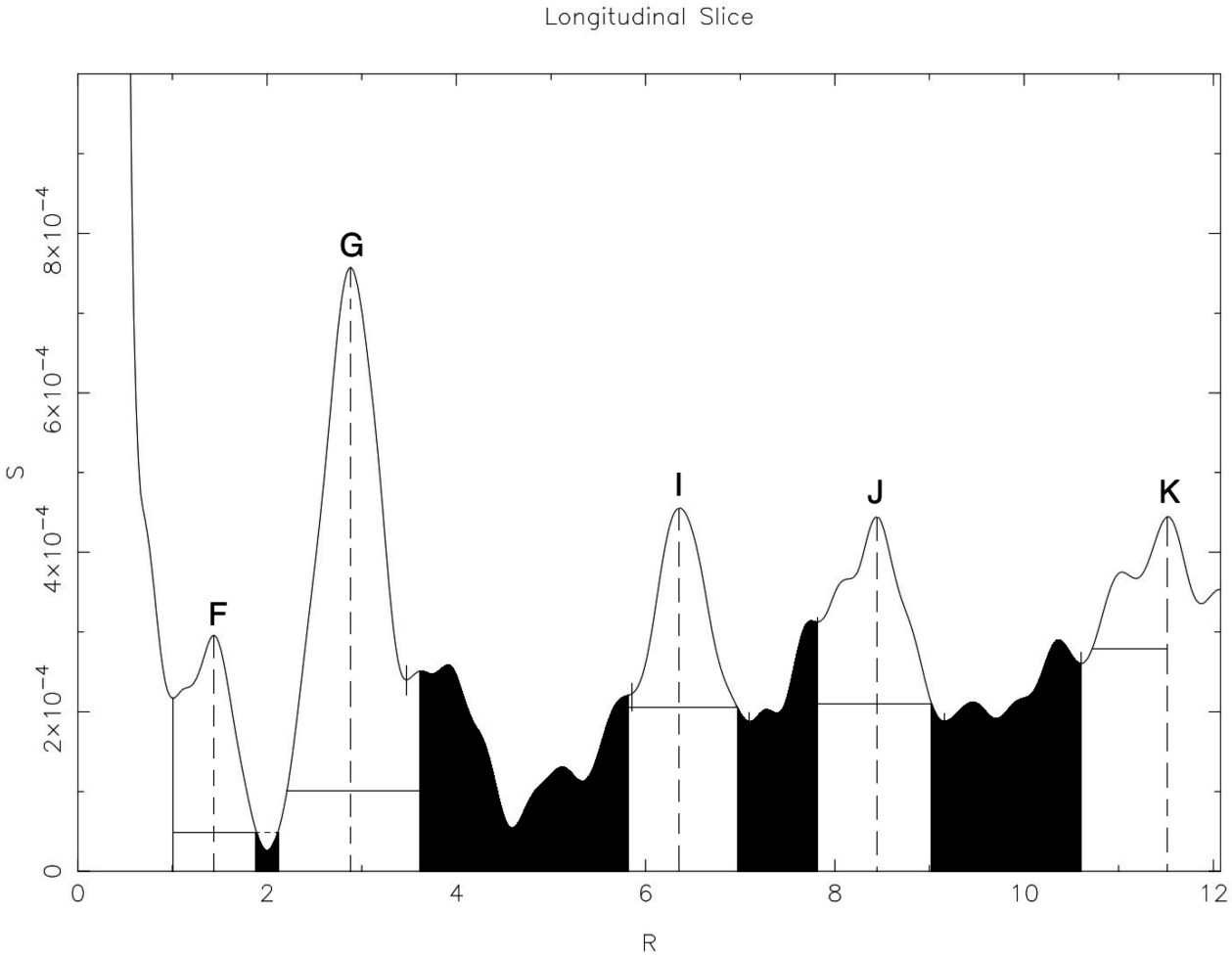

Figure 4.28: The longitudinal profile of 3C334. The strong feature on the left is the central feature, vertical dashed lines signify knot peak locations, horizontal solid lines signify 10% levels, small vertical solid lines signify 50% levels, horizontal dashed lines signify the use of rule 3b from above, and dark areas are interknot regions. The region between the central feature and knot F is undefined because the 10% level of knot F, when extended symmetrically across the peak of F, is past the minimum between the central feature and F. Thus, the interknot region in that section has no area and is undetermined.

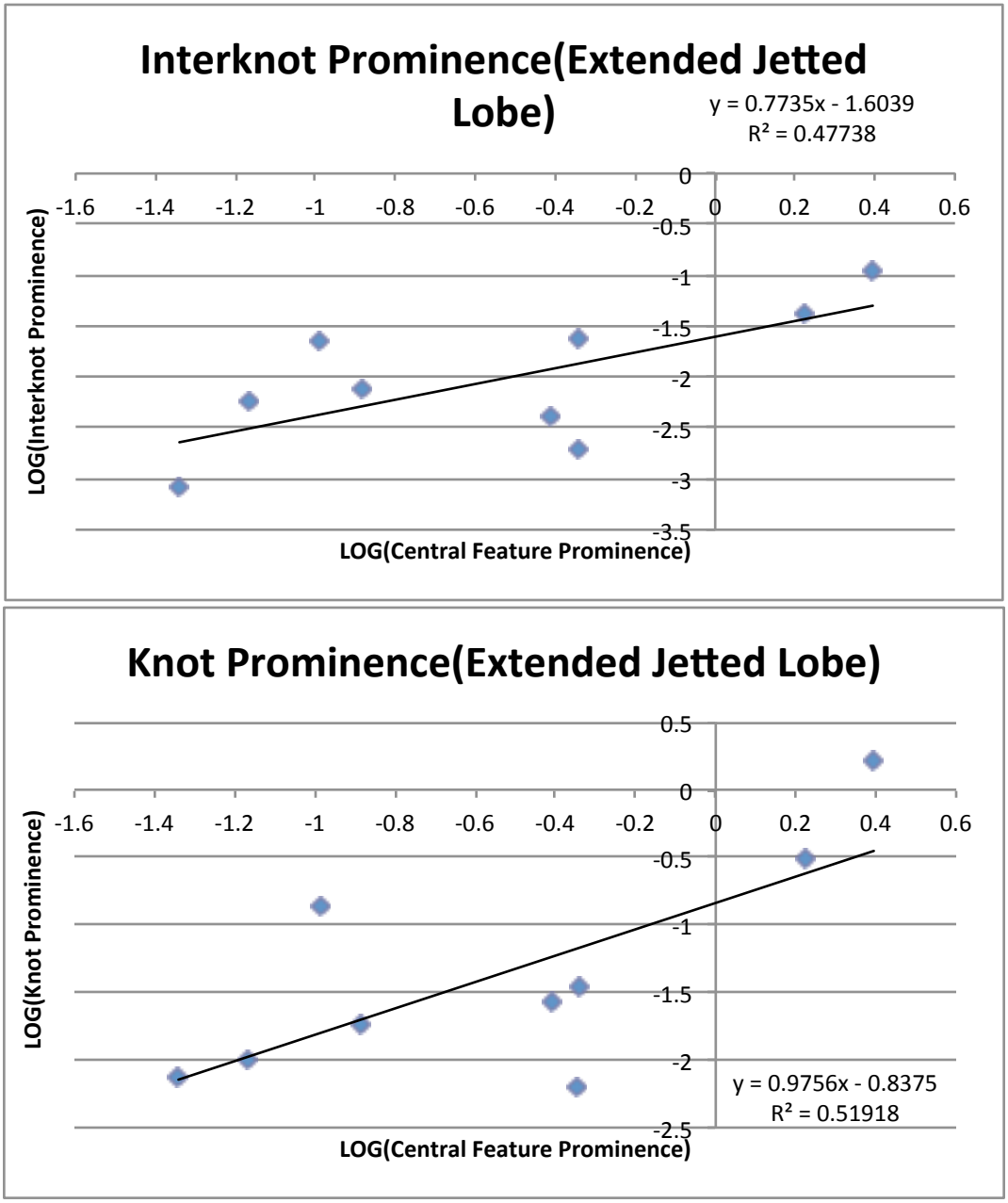

Figure 4.29: Interknot and knot prominences relative to the jetted lobe emission vs. central feature prominence.

fractions of total knot flux and total interknot flux in each of the four regions were plotted in Figure 4.30.

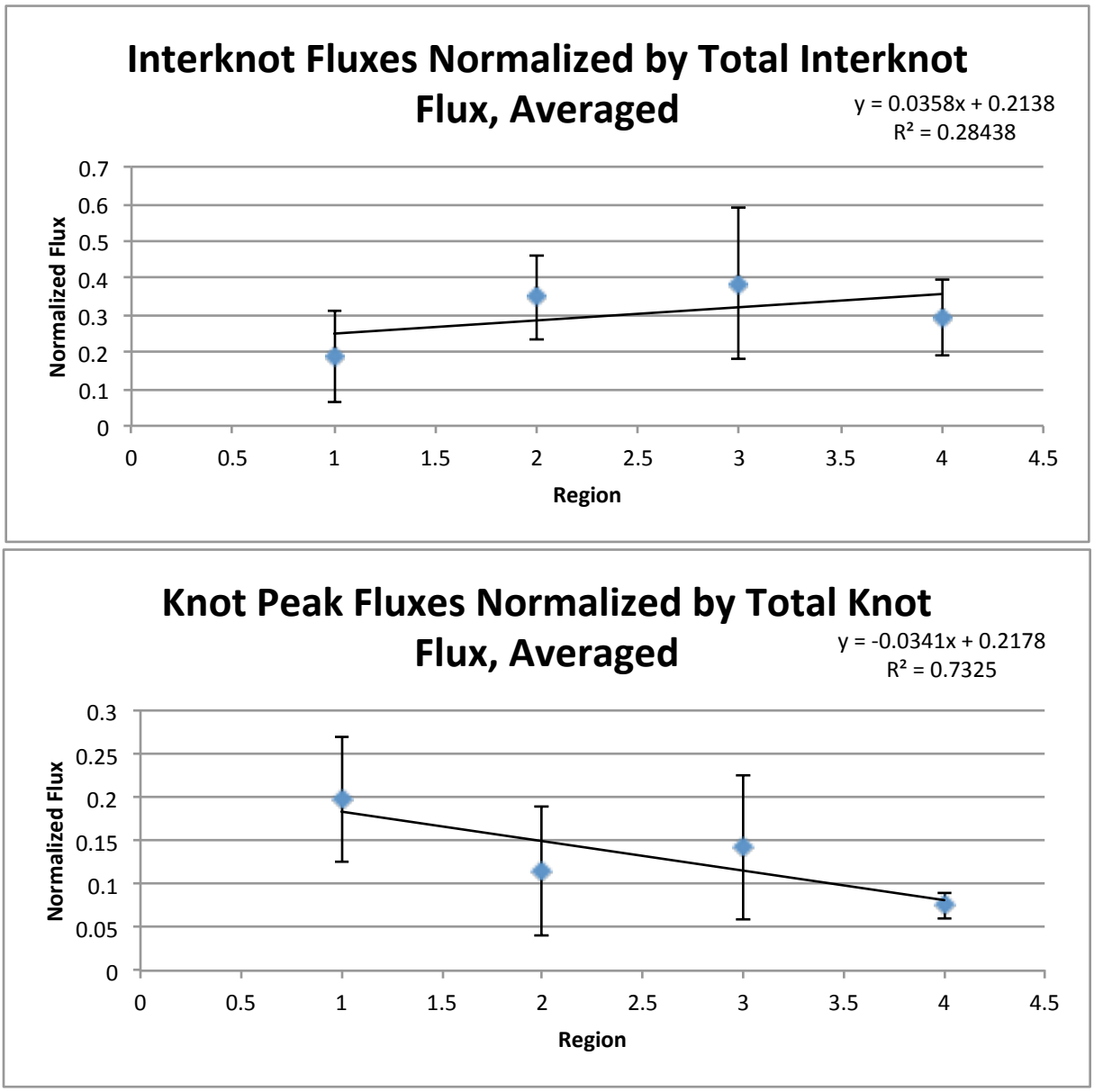

Figure 4.30: Average and standard deviation for interknot and knot flux densities in regions along the jet.

The unweighted uncertainties for the interknot and knot slopes are 0.036 ± 0.040 and -0.034 ± 0.015, respectively. Thus, the interknot slope is not significant, while the knot slope is marginally significant. A weighted least-squared fit for the knot flux density relationship, which emphasizes the small uncertainty of the fourth region, gives a slope of -0.036 ± 0.010, which is above 3σ and is thus significant.

4.5 Number Distributions of Jet/Counterjet Brightness Ratios

A jet moving with speed $v = \beta c$ will have a Doppler factor of $\delta = [\gamma(1 - \beta cos\theta)]^{-2.6}$, so a counterjet moving in the opposite direction with have a factor of $\delta = [\gamma(1+\beta cos\theta)]^{-2.6}$. After finding the ratio of these two factors, $J = (\frac{1-\beta cos\theta}{1+\beta cos\theta})^{-2.6}$, we were able to solve for the angle, $\theta = cos^{-1}(\frac{J^{-1/2.6}-1}{-\beta-\beta J^{-1/2.6}})$. The initial assumption was made that both the jet and counterjet have the same β and the angular distribution of jets to our line of sight is 0^o-90^o. Because the theoretical distribution is continuous, the probability of a source lying in an angle range θ_1 to θ_2 is $cos\theta_2 - cos\theta_1$. By assuming that the smallest observed jet/counterjet ratio is equal to the 90^o theoretical value for a range of possible values of β, we could create histograms (number distributions) of theoretical data and observed values. These histograms were then compared by calculating $\chi^2 = \Sigma((f_t - f_o)^2/f_t)$, which was summed over all histogram bins. Because most of the sources lacked counterjet candidates, a counterjet flux upper limit was found by integrating over the same area as the straight jet, but on the opposite side of the central feature. With a counterjet upper limit, only a lower limit of the jet/counterjet flux ratio could be found, so most of the sources could be moved to higher bins (see Figure 4.31). With this flexibility, most combinations of angles and values of β could be matched with the observed distribution. We found that $\gamma \geq 3$ is required to span the four orders of magnitude of the observed distribution, but a theoretical distribution with $\gamma = 2$ would be acceptable

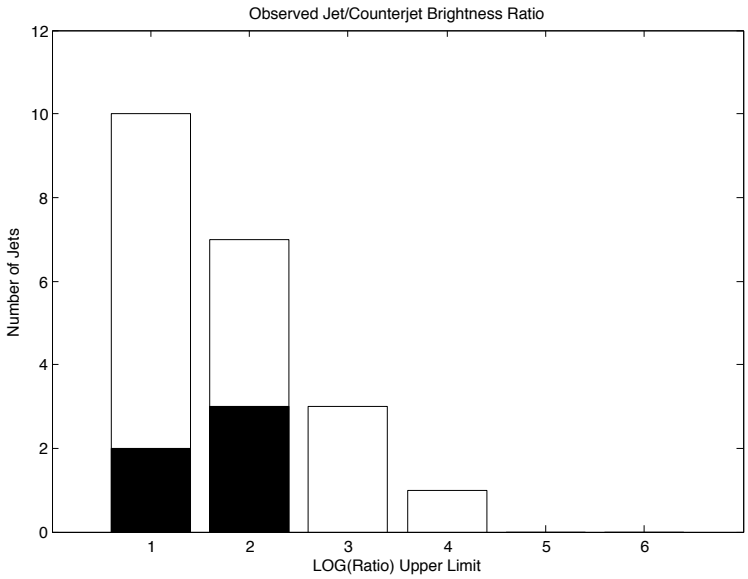

Figure 4.31: Observed jet/counterjet brightness ratio number distribution. Sources with counterjet candidates and thus counterjet flux estimates are darkened. White sources have counterjet flux upper limits and could be moved to higher bins to match a wide number of trial theoretical distributions.

if the highest observed source was excluded. A sample theoretical distribution is shown in Figure 4.32.

4.6 Number Distributions of Jet Brightness

Because of the lack of counterjet detections for most of the sources in the sample, the counterjet flux density upper limits were determined by arbitrarily assuming that we should integrate over the area between the central feature and the counterjetted hot spot. To avoid the ambiguity of the counterjet estimates, theoretical histograms of jet brightness were created and compared to observed jet flux brightnesses. The observed straight jet prominences span ~ 2.1 in the log, so we placed data into four bins of width 0.6 in the log. We then restricted theoretical distributions to those that did not predict prominences beyond the highest bin. For random orientations, the left edge of the first bin (smallest value

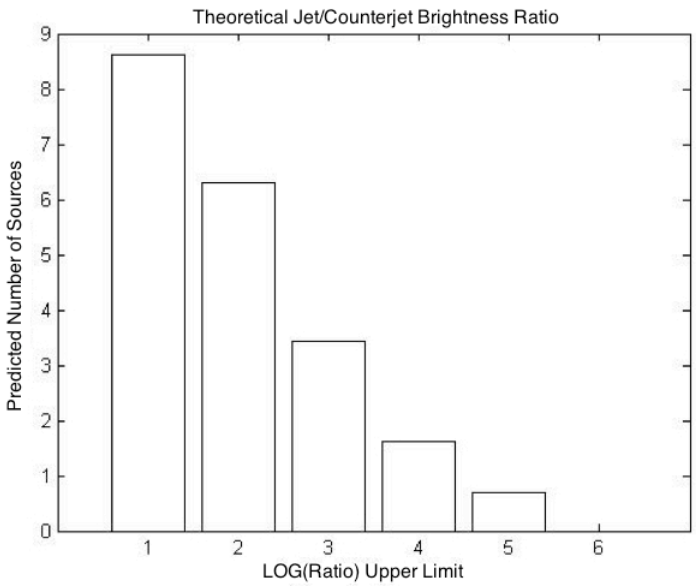

Figure 4.32: Theoretical jet/counterjet brightness ratio number distribution with $\gamma = 5$ and an angle range of 0^o to 90^o.

of log prominence) was set equal to the minimum observed log prominence. For restricted orientations, the left edge of the first bin was lowered to the value that would be observed for a jet at $\theta = 90^o$ and the observed distribution was shifted by the Doppler factor of the smallest theoretical angle. As shown in Figure 4.33, this shift required rebinning of sources, as some are near the bin boundaries.

We calculated theoretical distributions of jet brightness for three different models. The first consisted of a homogeneous jet with a single β. The second was a form of "spine-sheath" model, where the jet consisted of a fast moving spine surrounded by a slower sheath. To simulate this, fluxes from two jets with different values of β were added. The third was used to explore the effects of adding jets of different intrinsic strengths together. A number distribution with a certain β and angle range was created for each of four equally spaced values of intrinsic jet strength spanning one histogram bin. Figure 4.34 shows our observed

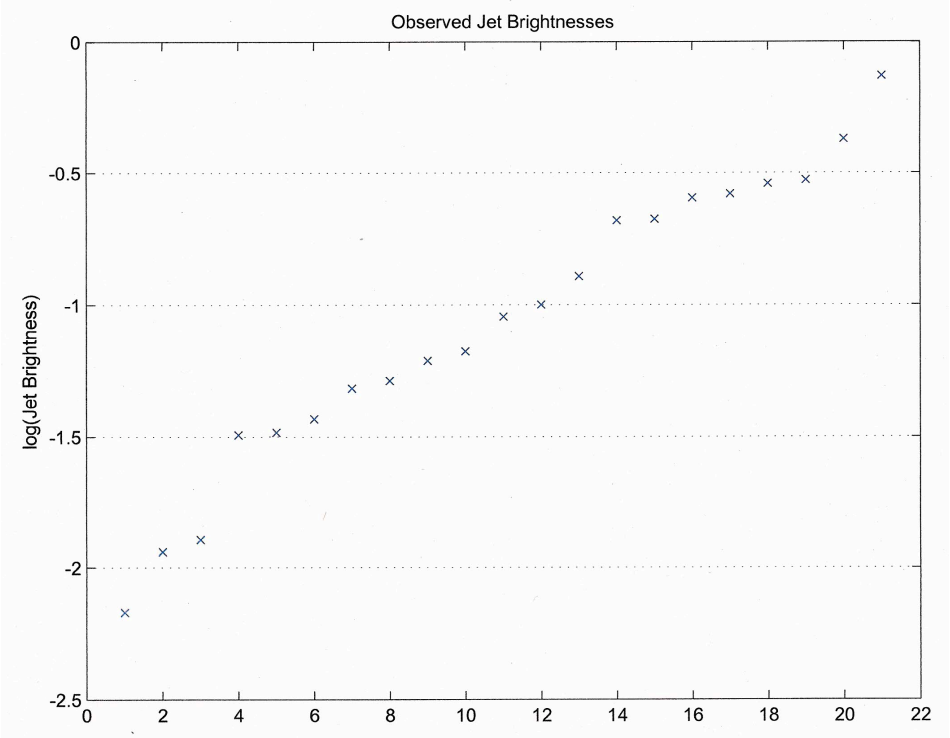

Figure 4.33: The distribution of jet brightness of sources in our sample. When compared to a theoretical distribution with a restricted angle range, the distribution could be shifted by < 0.6 in the log of the brightness. While this would not create a fifth bin for observed values, the number of sources in each bin may change due to their proximity to bin boundaries.

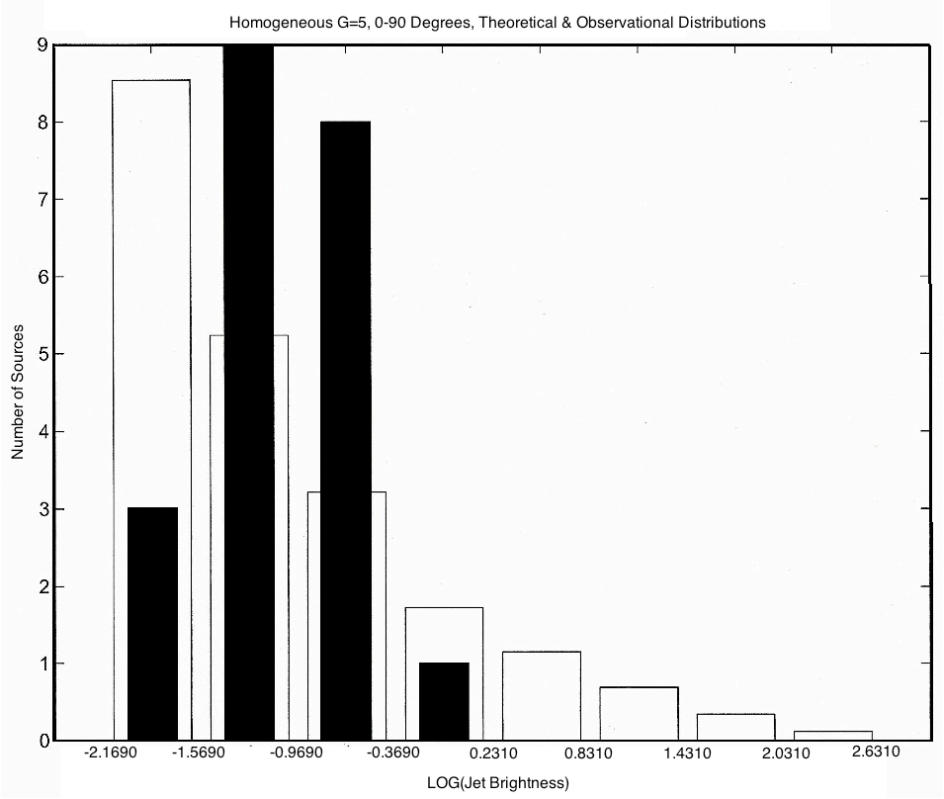

Figure 4.34: Histogram for observed values (darkened) and theoretical values (light) for a theoretical homogeneous jet with $\gamma = 5$ and angle range of 0^o to 90^o.

and theoretical histogram for a homogeneous jet with $\gamma = 5$ and angle range of 0^o to 90^o. While the theoretical distribution falls off monotonically, the observed distribution starts low, increases quickly, and decreases quickly. Thus, this theoretical distribution does not match the observed values. In addition, it extends way beyond the highest observed values. These distributions returned a χ^2 value of 16.03, which corresponds to a confidence level of $\sim 5\%$, further indicating a poor match to the observed values.

Because a shortened angle range would result in a shortened theoretical distribution and a shifted observed distribution, a Matlab code was created that would find the χ^2 value for all angle ranges that would not result in an infinite χ^2 value due to a observed value lying in a bin in which there were no theoretical values. In this way, the minimum χ^2 value for each

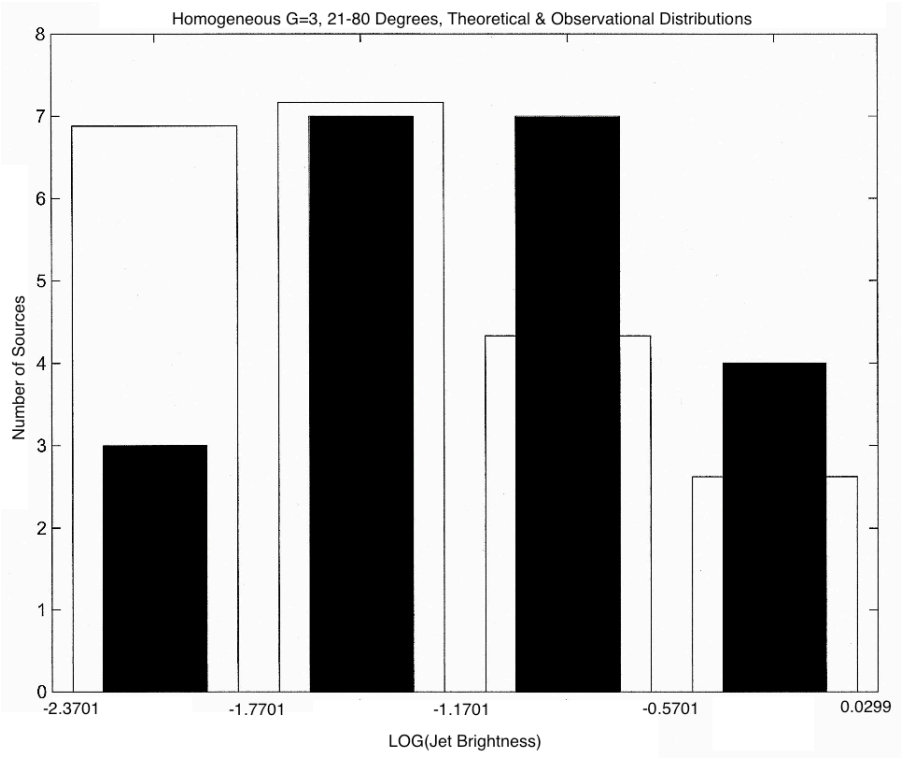

Figure 4.35: Histogram for observed values (darkened) and theoretical values (light) for a theoretical homogeneous jet with $\gamma = 3$ and angle range of 21^o to 80^o.

value of β was then found. Figure 4.35 shows the observed and theoretical distributions for a theoretical value of $\gamma = 3$ and the optimized angle range of 21^o to 80^o. Since the smaller angle range results in fewer theoretical bins, the theoretical and observed distributions are very similar. Despite the fact that the theoretical distribution increases slightly and decreases quickly while the observed distribution increases, remains constant, and decreases, the two distributions seem to match well. These distributions returned a χ^2 value of 4.56, which corresponds to a confidence level of $\sim 35\%$, so the theoretical distribution is consistent with the observed distribution.

The same procedure for our spine-sheath model was then followed, as shown in Figure 4.36. With this full angle range, the leftmost theoretical bin will be large and excess bins

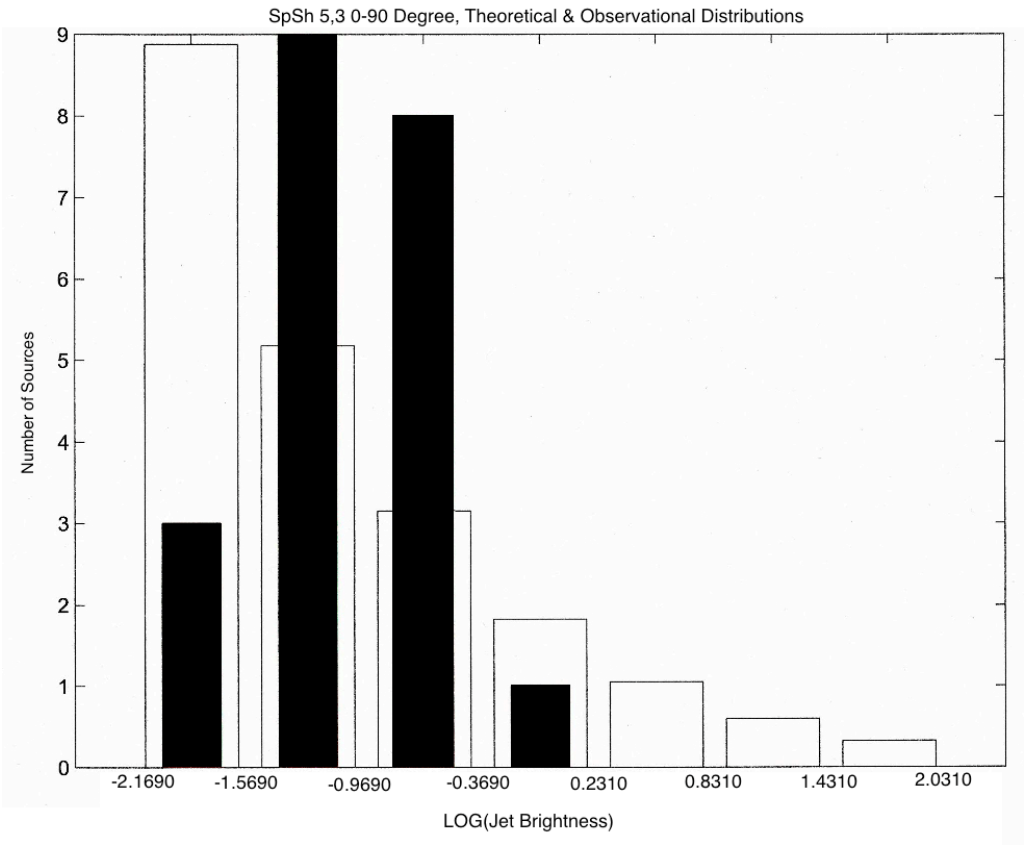

Figure 4.36: Histogram for observed values (darkened) and theoretical values (light) for a theoretical spine-sheath jet with $\gamma_{spine} = 5$, $\gamma_{sheath} = 3$, and angle range of 0^o to 90^o.

to the right will be present. Thus, this theoretical distribution is not a good match for the observed distribution. These distributions returned a χ^2 value of 16.522, which corresponds to a confidence level of $\sim 2\%$, showing that this theoretical distribution is inconsistent with the observed values.

In order to find a better match for the observed distribution, different angle ranges were tested. The smaller angle range and increased flexibility due to the spine and sheath allowed the theoretical distribution shown in Figure 4.37 to match the observed distribution quite well. These distributions returned a χ^2 value of 5.00, which corresponds to a confidence level of $\sim 25\%$, which shows that the distributions are consistent. As expected, unrestrained

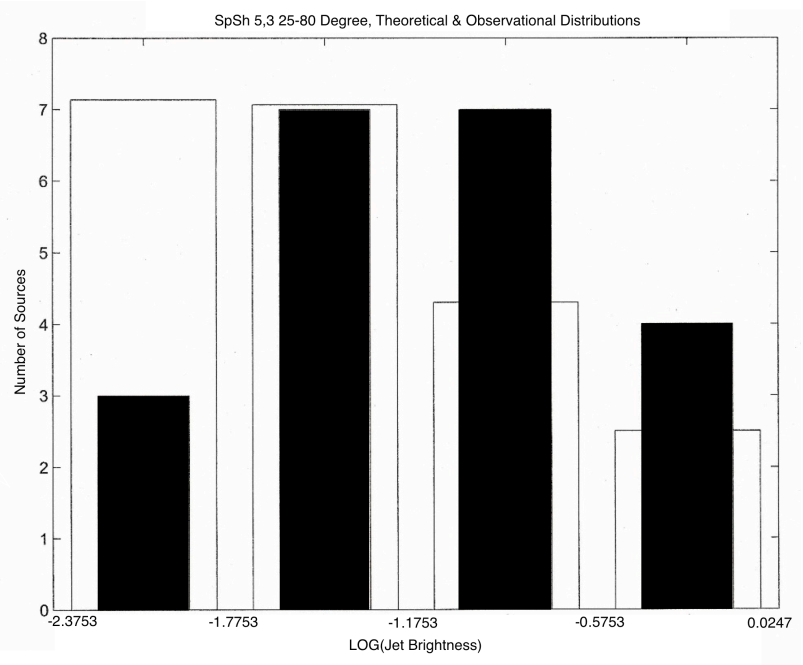

Figure 4.37: Histogram for observed values (darkened) and theoretical values (light) or a theoretical spine-sheath jet with γ_{spine} of 5, γ_{sheath} of 3, and angle range of 25^o to 80^o.

angle ranges returned high χ^2 values, while optimized angle ranges returned better fits. The best fit came from a theoretical spine-sheath jet with $\gamma_{spine} = 5$, $\gamma_{sheath} = 3$, and angle range of 25^o to 80^o, as shown in Figure 4.37.

Because the Matlab code did not work with distributions of intrinsic brightness, histograms with the same values for γ and the same angle ranges as for the homogeneous cases were produced. A distribution of brightnesses with $\gamma = 2$, an angle range of $0^o - 79^o$, and a leftmost bin edge value of -2.260 in the log produced a number distribution with confidence level of $\sim 60\%$, showing that such a theoretical distribution is consistent with the observed distribution. The other distributions, which included the full angle range distributions for $\gamma = 2$, 3, and 5 and the optimized angle range for $\gamma = 3$, produced number distributions with confidence levels of $\sim 40\%-$ $\sim 50\%$, all of which are consistent with the observed distributions. The histograms for the $\gamma = 5$ distributions with unoptimized (Figure 4.38)

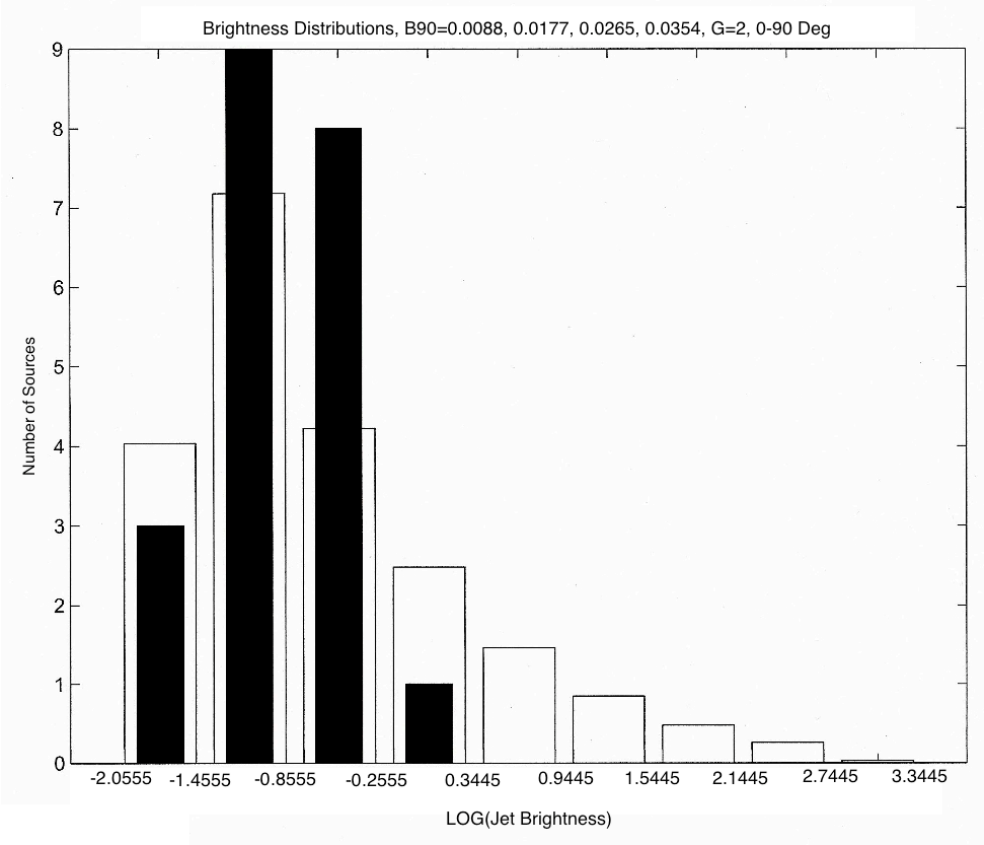

Figure 4.38: Histogram for observed values (darkened) and theoretical values (light) for a theoretical distribution of jets with γ of 5 and angle range of 0^o to 90^o.

and optimized (Figure 4.39) angle ranges are shown here.

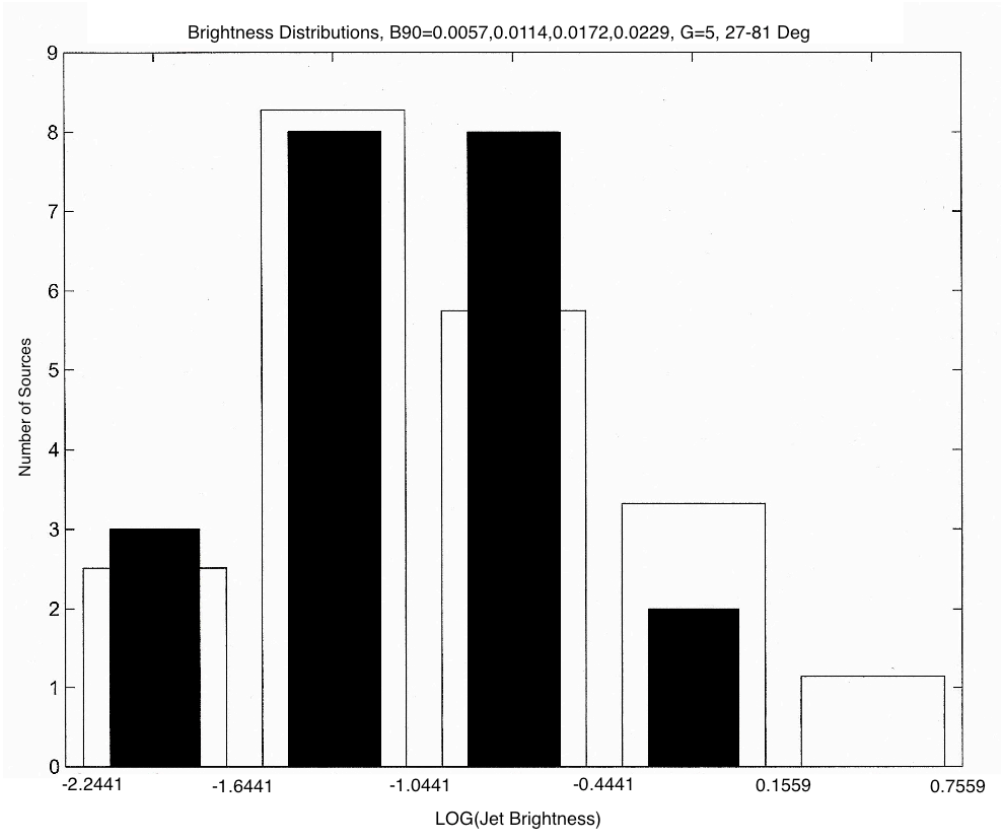

Figure 4.39: Histogram for observed values (darkened) and theoretical values (light) for a theoretical distribution of jets with $\gamma = 5$ and angle range of 27^o to 80^o.

4.7 Transverse Brightness Profiles

In order to place limits on the properties of the observed jets, we convolved spine-sheath models with Gaussian beams. It was assumed that the jet material was optically thin, so all emission was observed. Theoretical models were produced by finding the path length of different lines of sight through a spine and sheath with different relative sizes (Figure 4.40). Both the spine and sheath contribute to the apparent flux density per unit length along the line of sight, and these contributions were summed for each line for sight. Each theoretical jet was oriented at 90^o to our line of sight.

For the case of a sheath that occupies 20% of the jet radius and a highly beamed spine that is not visible, a central decrease in brightness in obvious, as shown in Figure 4.41.

The relative strength of the spine was then increased so that it had 10% of the apparent flux density per unit length of the sheath. This resulted in a flattening of the central brightness, as seen in Figure 4.42. As the relative strength of the spine continued to increase, the convolution assumed a more Gaussian shape, as in Figure 4.43.

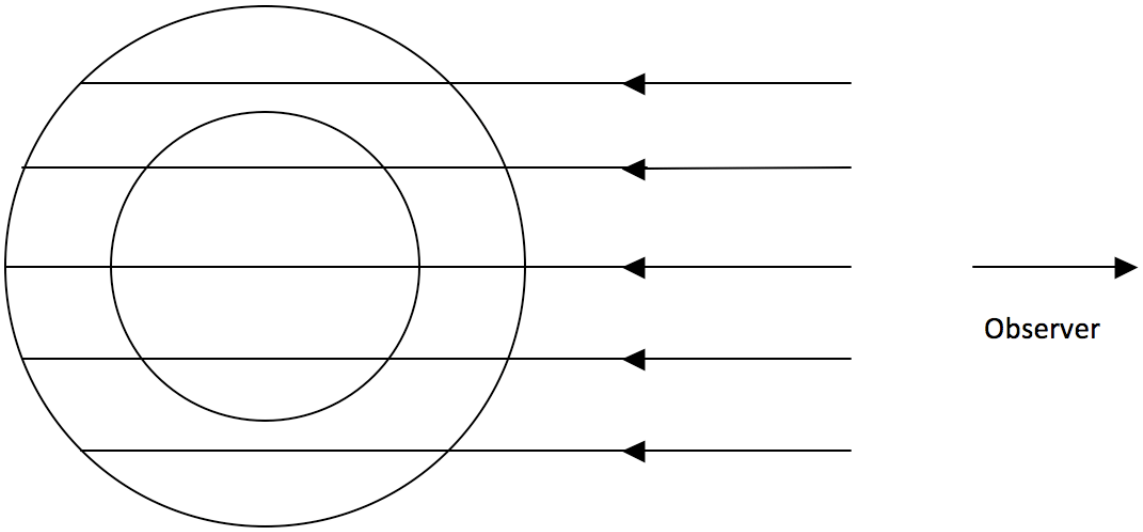

Figure 4.40: An illustration of our model construction. The inner circle on the left represents the boundary between the spine and sheath layer, while the outer circle marks the outer boundary of the sheath. Each horizontal line represents a line of sight along which the apparent flux density per unit length is integrated. For an observer far from an object, all lines of sight will be approximately parallel, as shown. Note that lines of sight closer to the center of the jet contain more contributions from the spine, while the extreme lines of sight contain more contributions from the sheath.

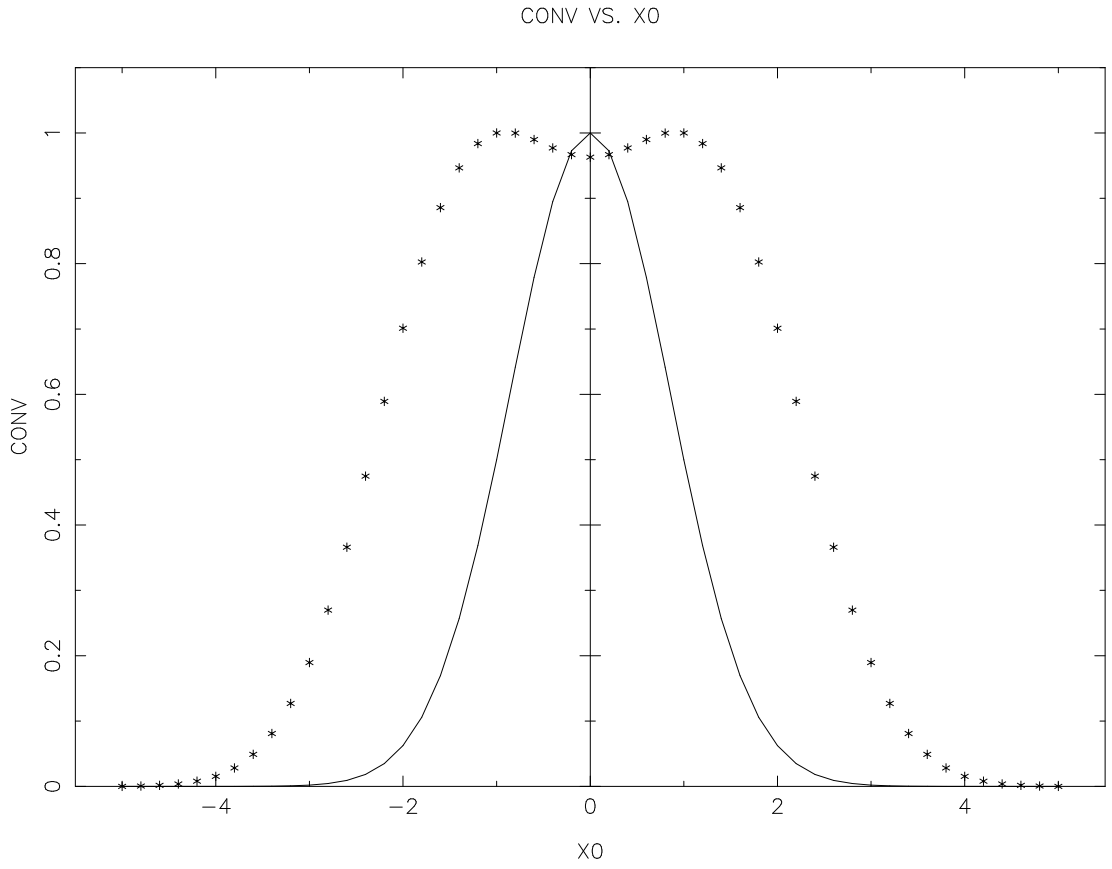

Figure 4.41: A convolution of a Gaussian beam and a spine-sheath model, where the asterisks mark the convolution and the solid line marks the beam. The radius of the sheath in the model is one fourth of the thickness of the spine. The spine is assumed highly relativistically beamed and thus invisible. A significant decrease in central brightness is observed.

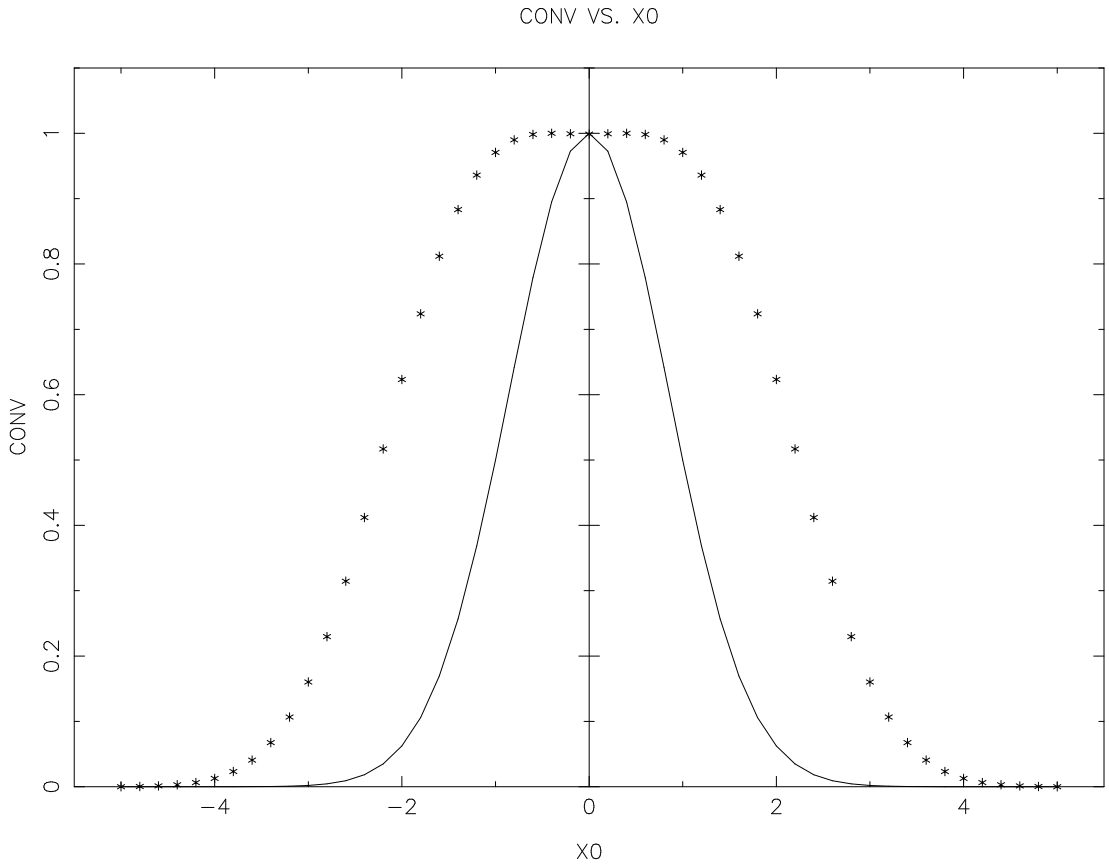

Figure 4.42: A convolution of a Gaussian beam and a spine-sheath model, where the asterisks mark the convolution and the solid line marks the beam. The radius of the sheath in the model is one fourth of the thickness of the spine. The apparent flux density per unit length of the spine is 10% that of the sheath. A broad area of constant brightness is observed.

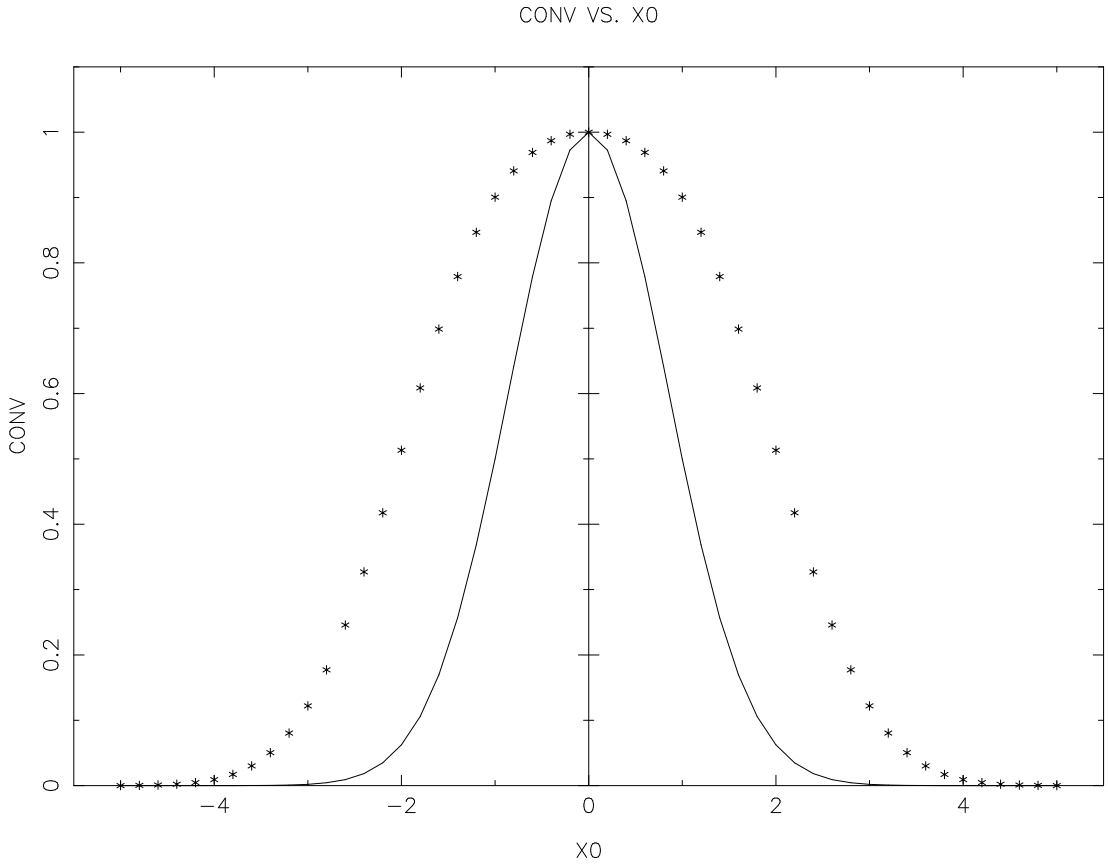

Figure 4.43: A convolution of a Gaussian beam and a spine-sheath model, where the asterisks mark the convolution and the solid line marks the beam. The radius of the sheath in the model is one fourth of the thickness of the spine. The apparent flux density per unit length of the spine is 30% that of the sheath. The convolution appears Gaussian.

5 Interpretation & Discussion

5.1 Source Structure

In their sample of thirteen 3CR lobe-dominated quasars, Bridle *et al.* (1994) found that all sources had jets, but only seven had counterjet candidates. In the eight additional sources that were added to this sample, all sources had jets, but no counterjet candidates were detected. A possible reason for this lack of detection is that the eight new sources are of smaller angular size and have stronger central features than the original thirteen, implying a smaller angle to our line of sight. This smaller angle would produce stronger beaming effects on kiloparsec scales, so the jet may appear brighter, but the counterjet would be less apparent, as observed.

5.2 Small- & Large- Scale Jet Connections

The positive slope of the straight jet-central feature prominence correlation, as seen in Section 4.2, implies a connection between the small- and large-scale kinematics of the jet. As the strength of the central feature increases, so does the strength of the straight jet. Thus, if the small-scale structure of the jet is moving relativistically and is beamed, the correlation can be explained if the large-scale jet also moves relativistically. This relationship has a slope of 0.58 ± 0.11 for the B condition with normalization by the extended emission of the jetted lobe.

In order to determine the speeds of the small- and large-scale structure of the jets, we plotted the logarithm of jetted emission S_j as a function of central feature emission S_c for a certain combinations of central feature and jet Lorentz factors γ_j and γ_c. Here, $S = (\gamma(1 - \beta cos\theta))^{-2+\alpha}$ with $\alpha_c = 0$ and $\alpha_j = 0.6$, so it was possible to compare our

observed prominence slope to the theoretical slope $m_{TH} = \frac{n+\alpha_j}{n+\alpha_c}\frac{\beta_j}{\beta_c}\frac{1-\beta_c cos\theta}{1-\beta_j cos\theta}$, where $n = 2$ for a continuous jet. If $\gamma_c = \gamma_j$, $m_{th} = 1.3$, which is more than twice the observed value. For $\gamma_c = 5$ and an angle range of 0^o to 90^0, a theoretical prominence relation that approximately matched the range of observed prominences with average slope 0.59 was found for $\gamma_j = 1.74$. For $\gamma_c = 10$ and an angle range of 10^o to 80^o, chosen to approximately match the observed prominence range, a theoretical prominence relation with average slope 0.58 was found for $\gamma_j = 1.75$. These fits are displayed in Figure 5.1.

It should be noted that while these theoretical prominence relations are represented by curved lines, we use their average slope for comparison to linear fits to the data (Section 4.2). Since the observed values have large scatter and show no obvious curvatures, only a linear fit is justified.

While these theoretical correlations do not determine a specific pair of central feature and jet Lorentz factors, the resulting relations are consistent with slower jet motion on the large scale. However, it is not yet clear if this deceleration occurs abruptly on intermediate scales or progressively on the kiloparsec scale. This deceleration will be explored further in the division of the jet into knots and interknot regions in Section 5.4.

It is important to check if other source properties might play a role in causing the correlation. Sources were identified as having either high or low ratios of hot spot distance and lobe extent to determine if either the recession of a hot spot or extent of a lobe were related to either prominence, which would be seen as a clustering of sources into two groups on the prominence plot. Because this grouping was not observed, there is no evidence that these properties affect the prominence correlation.

Sources were also split into groups with and without detected counterjet candidates. While the sources with counterjet candidates and high counterjetted hot spot recession ratios have a stronger correlation - which remains a mystery - the groups have similar slopes and

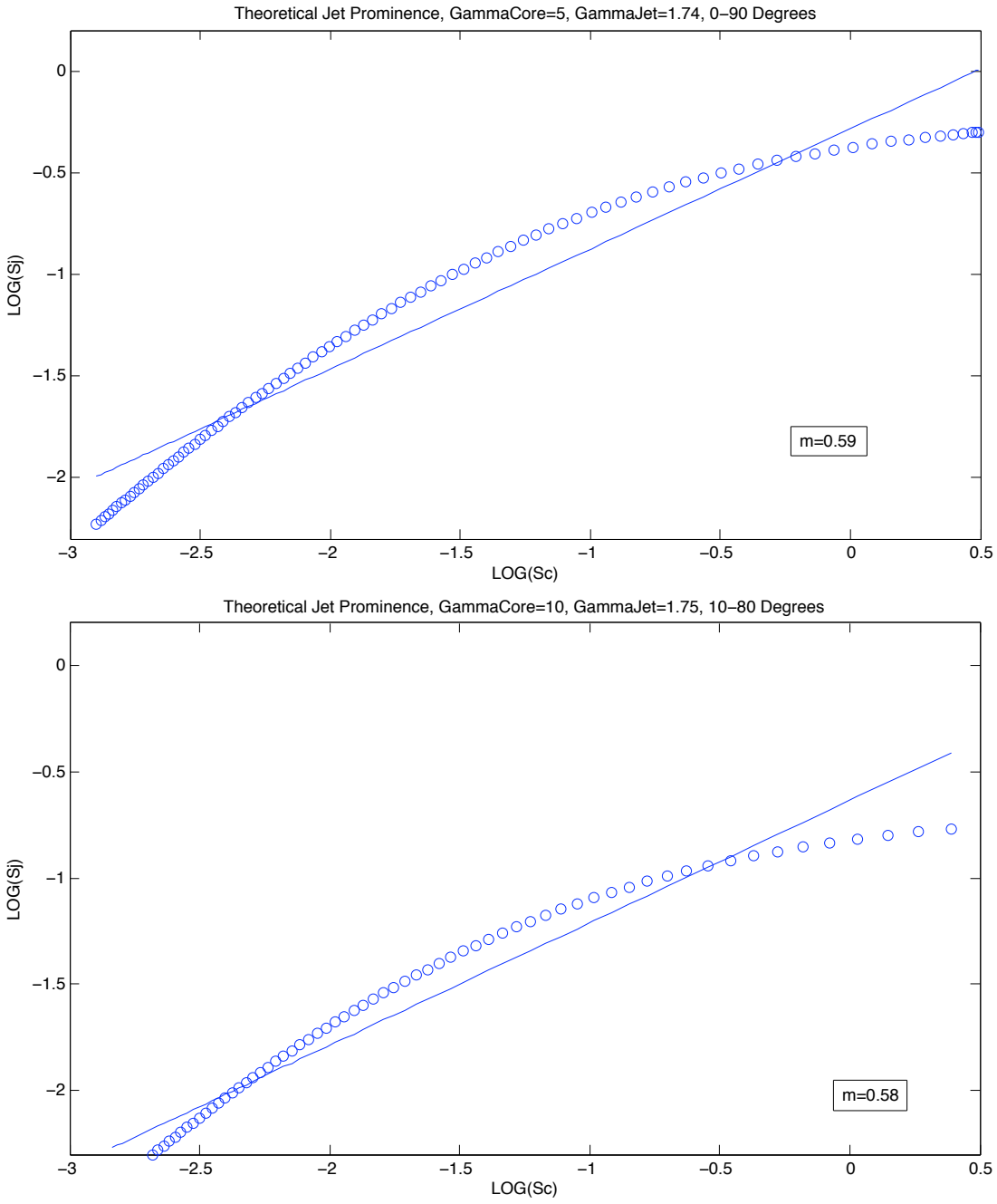

Figure 5.1: Theoretical prominence relation, displayed in circles, and its best linear fit for $\gamma_c = 5$ and $\gamma_c = 10$. The best linear fit for the observed sources gave a slope of 0.58 ± 0.11, so both of these theoretical relations match observations. The angle range for $\gamma_c = 10$ was reduced to match the range of the observed straight jet prominence.

show no clusters, so the presence of a counterjet candidate or a high ratio does not influence the prominence correlation.

There is also no evidence that redshift affects the prominence correlation, as low and high redshift groups show no clustering.

For a quasar with diametrically opposed jets, the hot spots would form on either side of the central feature such that the misalignment angle (see Section 4.1.1) was 0^o. However, the observed quasars have bent jets and off-axis lobe structure, so the misalignment angle can be large. Although the counterjet is usually completely invisible, the counterjetted hot spot may be misaligned compared to the jetted hot spot. Identification of sources as having either small or large misalignment angles does not result in clustering on the prominence plot, so this also has no effect on the correlation. Additionally, the existence of a coherent sequence of knots has no effect.

5.3 Jet Bend Angle - Hot Spot Prominence Relation

Of the three jet bend angles, η_{2C} showed the strongest bend angle - hot spot prominence anticorrelation. However, this anticorrelation is dependent on one source, 3C215, with extreme properties. This source has one of the two highest misalignment angles, the smallest jetted hot spot/counterjetted hot spot distance ratio, the smallest jetted hot spot recession ratio, the second largest value of η_{2C}, the second smallest redshift, and the weakest jetted hot spot. Since omission of this one source would reduce the anticorrelation to below the 90% confidence level, it cannot be claimed that strong jet bending reduces the ability to form a strong hot spot. Because the majority of jets had some significant bending ($\eta_{2C} \geq 5^o$), this means that organized flow is maintained during direction change, even in the case of the highest observed bending.

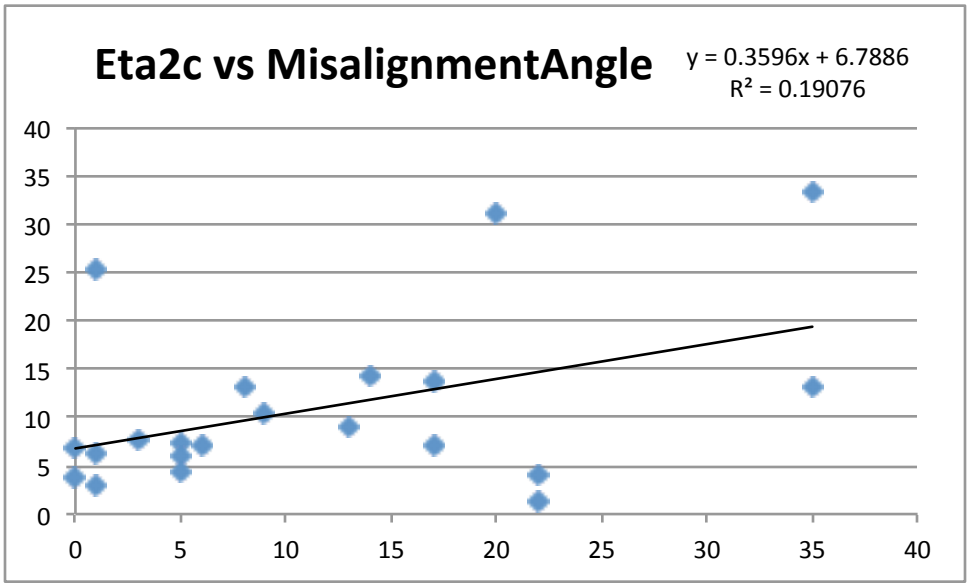

Figure 5.2: Largest angle between jet features as a function of misalignment angle. The slope of 0.36 ± 0.17 is above 2σ, so the correlation is marginal (confidence level $\approx 95\%$).

It was thought that jets that bend strongly would exhibit a large misalignment angle due to movement orthogonal to the original jet direction. As shown in Figure 5.2, there may be a marginal correlation. While the jets may oscillate or "wiggle" slightly, they ultimately bend in one direction at large distances from the central feature. A possible reason for the weakness of this correlation is the "S-symmetry" of sources, where the counterjet exhibits the opposite bending behavior of the jet, causing the misalignment angle to be small. Alternatively, jets may bend in one direction and reverse, causing a large η_{2C} but minimizing the misalignment angle.

5.4 Interknot Emission

In order to investigate the longitudinal velocity field in the jet, we focused on the interknot regions, which best represent underlying flow away from shocks in the knot complex. Initial attempts to measure interknot emission from 3C263 and 3C334 were not well-defined and

yielded no evidence for a correlation of interknot flux with distance along the jet.

In order to determine the behavior of interknot flux, we adopted a systematic definition of knot complex borders and expanded our sample to nine sources with quasi-periodic knot patterns. These sources are all well-distributed along the straight jet - central feature prominence correlation. We found that the prominences of the total knot and total interknot emission correlate with the prominences of the central features. This shows that the knot and interknot regions are each separately beamed. The slopes of the knot prominence relation (0.98 ± 0.35) and interknot prominence relation (0.77 ± 0.31) are nominally larger than the straight jet prominence correlation (0.58 ± 0.11). However, the slopes all agree within the quadrature uncertainties.

The next step was to examine the emission of the individual knot and interknot regions as a function of position along the jet. There were no consistent trends displayed by individual sources, so instead we formed a composite profile for all nine sources as a function of position (first knot, second knot, etc.). The interknot profile is consistent with zero slope, so there is no evidence for systematic brightness changes of the underlying continuous flow along the jet. However, the knot profile showed a significant decline in knot strength as the jet progressed. Thus, while the underlying flow was unaffected by distance from the central feature, the knot disturbances weakened. This may mean that the mechanism that causes shocks is initially strong near the central feature, but exhibits a decline in strength with distance. For example, if shocks are formed by faster material encountering slow material, pre-shock material far from the central feature may be slowed by prior interaction with jet material and thus form weaker disturbances.

Additionally, we tested the effect of the "knot dominance" of the jet (*i.e.*, the ratio $\frac{KnotEmission}{JetEmission}$) on the distribution of sources in the prominence relation. In percentage terms, the values corresponding to these ratios for our nine sources are :

1	3C212	94%	6	3C263	76%
2	3C205	90%	7	3C204	70%
3	3C207	88%	8	3C175	65%
4	3C208	87%	9	3C334	59%
5	4C16.49	86%			

Table 5.1: The ratio of knot emission to jet emission in percentage terms for our nine sources.

However, no correlation between knot dominance and prominence plot position was observed. Thus, the mechanism that causes knots to have a dominant share of the emission is unrelated to beaming, and must have something to do with detailed shock physics.

5.5 Jet/Counterjet Brightness Ratio

The distribution of observed jet/counterjet brightness ratios includes seven sources with counterjet candidates and fourteen sources without detected counterjets. Thus fourteen sources have only lower limits on jet/counterjet ratios, meaning that they could readily be assigned to higher bins to match a wide range of theoretical distributions. This makes it difficult to draw definitive conclusions. The range of jet/counterjet ratios for sources with counterjet candidates requires a Lorentz factor of ≥ 3 for random and restricted orientation ranges, but a Lorentz factor of 2 would work if the source with the largest ratio was excluded. This may explain the lack of counterjets, as the anisotropic light cone would be pointed away from the observer, placing the majority of counterjets below our detection threshold.

5.6 Jet Brightness Distributions

The goal of investigating the number distribution of theoretical jet prominence was to find Lorentz factors and angle ranges consistent with the observed distribution. Out of our theoretical models, homogeneous jets with identical rest frame brightness, $\gamma = 3$, and angle range of 21^o to 80^o give the best match to the observed distribution. For a jet with a spine and sheath with identical intrinsic brightness, the best result came from a distribution with $\gamma_{spine} = 5$, $\gamma_{sheath} = 3$, and angle range of 25^o to 80^o. For homogeneous jets with a range of rest frame brightness, theoretical distributions using the same γ and angle range of optimized homogeneous distributions were acceptable, but distributions with $\gamma = 2$ and $0^o - 79^o$ gave the best fit. Homogeneous and spine-sheath jet distributions with random orientations were ruled out. Thus, while some cases do not fit the data, acceptable fits for all three jet models show that the jets may range in complexity from a sample of homogeneous jets to multi-layer jets to jets of different intrinsic strengths.

While we cannot rule out any of the three models on the basis of our jet brightness results, other lines of investigation (e.g. Laing & Bridle 2002) strongly suggest that homogeneous jet models are inadequate. So while it is not possible from this investigation to place strong constraints on velocity fields and orientation ranges of our sample, we have at least been able to rule out some regions of parameter space for inhomogeneous jet models, and to show that acceptable $\gamma = 2$ distributions can be found that are consistent with $\gamma = 2$ from the prominence correlation.

5.7 Transverse Jet Profiles

The goal of our convolutions was to create theoretical profiles that could be compared to observed transverse profiles in order to rule out models inconsistent with the observations.

When jet models that were only one beam wide or Gaussian were used, the resulting profile was not distinct from a Gaussian. By using an invisible spine and thin sheath and a model two beams wide, a distinctly non-Gaussian profile was created. As the relative apparent flux density per unit length of the spine increased, the profile more approximated the shape of the beam. In the cases of spines with zero or low apparent flux densities, the resulting profile diverged from Gaussian behavior. Of the transverse profiles taken from jet observations so far, the widest jets are around two beams wide and are Gaussian in appearance. Thus, spines with low apparent flux density and jet profiles that are two beams wide are ruled out on the grounds that they do not represent what is observed.

It is not yet clear if the apparent flux density of the spines would be a result of intrinsic properties or Doppler beaming. It is thought that the sheath may exhibit a higher apparent flux density as a result of radiation loss through interaction with the surrounding medium at the border of the jet. For a spine and sheath with identical intrinsic emissivities and Lorentz factors of 5 and 2, respectively, the ratio $\frac{\delta_5}{\delta_2}$ ranges from 0.4 at 90^o to 2.7 at 0^o. In the more extreme case of $\gamma_{spine} = 10$ and $\gamma_{sheath} = 2$, this ratio ranges from 0.2 at 90^o to 5.4 at 0^o. Thus, beaming may greatly affect the apparent flux density per unit length of the spine and sheath.

However, this analysis was performed only with theoretical jets at 90^o to our line of sight, so no relativistic corrections for path lengths were made. Because we know that our sample contains jets at a range of angles, these corrections could be made to place further limits on the transverse structure of the jets.

6 Conclusion

The addition of eight quasars to the thirteen of Bridle *et al.* (1994) allowed past analyses to be re-examined and new analyses to be performed. One such analysis, the examination of hot spot prominence as a function of bend angle, was found to rely on a single source with bizarre structure and was not supported by the expanded sample. The prominence of the straight jet as a function of central feature prominence showed that the small-scale behavior of the jet is connected to the large-scale behavior. Since the jets are known to be highly relativistic at the level of the central feature, the beaming interpretation indicates that the kiloparsec-scale jets are also relativistic, although decelerated to $\gamma \sim 2$. In a subsample of nine sources, it was found that this beaming is communicated separately by both the knots and interknot regions. The strength of the underlying flow showed no systematic variation along the jet, consistent with no further deceleration on kiloparsec scales. The strength of knot peaks was found to decrease with distance from the central feature, but this weakening of the shocks conveys no clear message about velocities of the knots. The knot dominance of the jets cannot be explained by beaming effects. The distributions of jet brightness for identical homogeneous jets support jets with $\gamma_j \geq 2$. Thus, both the straight jet-central feature prominence correlation and jet brightness number distributions argue for jet deceleration between parsec and kiloparsec scales ($\gamma_j \sim 2$). The observed jet/counterjet brightness ratio only matched well to theoretical distributions with $\gamma \geq 3$, but a distribution with $\gamma = 2$ would be acceptable if the source with the highest ratio was removed.

We also investigated distributions for a spine-sheath model and a model with a range of intrinsic brightnesses. The former yielded a set of optimized angle ranges ($25^o - 80^o$) with acceptable agreement with observations, and showed that models assuming random orientations give poor fits to the data. This is consistent with unified models for active

galaxies that place lobe-dominated quasars in an intermediate angle range. By comparing theoretical convolutions of a Gaussian beam with different spine-sheath models, very fast and/or very low emissivity spines were ruled out.

It should be noted that our sample did not consist of 21 quasars with identical detailed properties. For example, the number of knots in the straight jet varies from one to five and some jets have regular knot patterns, while other jets consisted of only one blob in an otherwise invisible flow. But they do share common defining elements, so our purpose was not to model the detailed behavior of a single source, but to improve upon the common model of this classification of quasar. After all, while their detailed properties may differ, they are all classified as 3CR lobe-dominated quasars (although 3C215 may warrant a different classification) and thus contain common structures and processes that generate their observable, basic features.

Further work on this sample will include analysis of the polarization data of these sources. These could be used to examine the magnetic field structure of each feature, including relativistic effects on fields in the jets. In addition, the EVLA may be used to image one promising source to attempt detection of a continuous counterjet.

References

[1] Benford, G. 1983, *Astrophysical Jets; Proceedings of the International Workshop, Turin, Italy*. D. Reidel Publishing Co., Dordrecht, p. 271.

[2] Blandford, R. D. & Rees, M. J. 1974, MNRAS, 169, 395

[3] Burke, B. F. & Graham-Smith, F. 2010, *An Introduction to Radio Astronomy*. Cambridge University Press, New York, Third Edition.

[4] Bridle, A. H., Hough, D. H., Lonsdale, C. J., Burns, J. O., and Laing, R. A. 1994, ApJ, 108, 766

[5] Carroll, B. W. & Ostlie, D. A. 2007, *An Introduction to Modern Astrophysics*. Addison Wesley, San Francisco, CA.

[6] Ghigo, F. 2008, *Karl Jansky and the Discovery of Radio Waves*. National Radio Astronomy Observatory. `http://www.nrao.edu/whatisra/hist_jansky.shtml`

[7] Jianjun, J. 2007, *Synthesis Imaging of Space Interferometry Mission: Complex Visibility*. Johns Hopkins University. `http://www.pha.jhu.edu/~jiajj/presentation/SIM_html/SIM/node4.html`

[8] Kembhavi, A. K. and Narlikar, J. V. 1999, *Quasars and Active Galactic Nuclei: An Introduction*. Cambridge University Press, Cambridge, UK.

[9] Laing, R. A. & Bridle, A. H. 2002, MNRAS, 336, 328

[10] O'Dell, S. L. 1981, ApJ, 243, L147

[11] Price, A. 2010, *BL Lacertae*. American Association of Variable Star Observers. `http://www.aavso.org/vsots_bllac`

[12] Rees, M. J. 1978, MNRAS, 184, 61

[13] Romney, J. D. 2012, *Very Long Baseline Array Observational Status Summary*. Chapter 8, National Radio Astronomy Observatory. http://www.vlba.nrao.edu/astro/obstatus/current/node24.html

[14] Shepherd, M. C. 1997, *Difmap: An Interactive Program for Synthesis Imaging*. ASP Conference Series, Vol. 125. http://www.cv.nrao.edu/adass/adassVI/shepherdm.html

[15] Stawarz, L., Sikora, M., Ostrowski, M., and Begelman, M. C. 2004, ApJ, 608, 95

[16] Thompson, A. R., Clark, B. G., Wade, C. M., and Napier, P. J. 1980, ApJS, 44, 151